Acta Biomaterialia 218 (2026) 542–558

Contents lists available at ScienceDirect

Acta Biomaterialia

journal homepage: www.elsevier.com/locate/actbio

Full length article

Membrane-anchoring naphthalimide-based aggregation-induced emission photosensitizers for NIR fluorescence imaging and photodynamic elimination of multidrug-resistant bacteria

Sayed Mir Sayed [a,*], Zeeshan Tahir [b], Yavuz Nuri Ertas [a,c,**]

[a] ERNAM–Nanotechnology Research and Application Center, Erciyes University, Kayseri 38039, Türkiye
[b] Department of Medical Biochemistry, Faculty of Medicine, Erciyes University, Kayseri 38039, Türkiye
[c] Department of Biomedical Engineering, Erciyes University, Kayseri 38039, Türkiye

ARTICLE INFO

Keywords:
Aggregation-induced emission
Antibacterial photodynamic therapy
Membrane targeting
Multidrug-resistant bacteria
Wound healing

ABSTRACT

Multidrug-resistant (MDR) bacterial infections demand antibacterial strategies that circumvent conventional resistance pathways and enable localized action with minimal host toxicity. Photodynamic therapy (PDT) represents a non-invasive approach; however, its effectiveness is constrained by insufficient bacterial targeting, aggregation-caused quenching, and limited reactive oxygen species (ROS) generation under physiological conditions. Herein, we develop two membrane-anchoring naphthalimide-based aggregation-induced emission (AIE) photosensitizers, TPAPV-NIM-mPy-M and TPAPV-NIM-Py-M, engineered via a donor–π–acceptor molecular design to integrate near-infrared (NIR) fluorescence imaging and antibacterial PDT. Both photosensitizers display visible-light absorption, pronounced AIE characteristics, and NIR emission, providing bright signals upon aggregation and facilitating rapid bacterial visualization. Under low-intensity white-light irradiation, they efficiently generate ROS via both type I and type II pathways, supporting oxygen-dependent and partially oxygen-tolerant mechanisms. The introduction of cationic pyridinium units promotes rapid bacterial binding and membrane-specific localization in Gram-positive and Gram-negative bacteria, thereby confining ROS at the bacterial envelope and enhancing photoinactivation. Notably, TPAPV-NIM-Py-M, benefiting from extended π-conjugation and stronger intramolecular charge transfer, exhibits higher ROS output and superior antibacterial efficacy against *Escherichia coli* (*E. coli*), *Staphylococcus aureus* (*S. aureus*), vancomycin-resistant *Enterococcus faecium* (VR *E. faecium*), and multidrug-resistant *Escherichia coli* (MDR *E. coli*), while maintaining negligible dark toxicity. Cytotoxicity and hemolysis assays confirm a favorable biocompatibility profile. TPAPV-NIM-Py-M also shows strong antibiofilm activity. Furthermore, TPAPV-NIM-Py-M enables effective *in vivo* photodynamic elimination of bacteria in an *E. coli*-infected wound model, significantly accelerating wound closure and tissue regeneration without systemic toxicity. This work establishes a membrane-targeted molecular engineering strategy for high-performance AIE photosensitizers and highlights their potential for image-guided photodynamic treatment of MDR bacterial infections and infected wounds.

Statement of Significance: Antibiotic resistance and biofilm-associated infections are driving demand for non-antibiotic antibacterial therapies. This study introduces naphthalimide-based aggregation-induced emission photosensitizers that anchor to bacterial membranes, enabling near-infrared fluorescence imaging and localized generation of reactive oxygen species for photodynamic killing. Membrane targeting improves efficacy against both Gram-positive and Gram-negative pathogens, including multidrug-resistant strains, and supports treatment of infected wounds in vivo with good biocompatibility. The work provides a general molecular design strategy for image-guided antimicrobial photodynamic therapy.

* Corresponding author at: ERNAM–Nanotechnology Research and Application Center, Erciyes University, Kayseri 38039, Türkiye.
** Corresponding author at: Department of Biomedical Engineering, Erciyes University, Kayseri 38039, Türkiye.
E-mail addresses: sayed.mir.sayed5@gmail.com (S.M. Sayed), yavuznuri@gmail.com (Y.N. Ertas).

https://doi.org/10.1016/j.actbio.2026.06.014
Received 16 February 2026; Accepted 5 June 2026
Available online 6 June 2026

1. Introduction

Humans and bacterial communities have a complex relationship; on the one hand, we benefit from beneficial bacteria, which can act as probiotics and help digest complex food particles and regulate the immune system, while on the other hand, pathogenic bacteria cause disease by overcoming host defense mechanisms that threaten our health and lives [1]. It has also been reported that members of the bacterial community living in the human gastrointestinal tract are responsible for several metabolic disorders and immune-mediated diseases, including inflammatory bowel disease, obesity, malnutrition, and anticancer immunity [2]. Due to the differences in membrane components, bacteria have been classified into two broad classes: Gram-positive and Gram-negative. The bacterial envelope differs markedly between Gram-positive and Gram-negative species. Gram-positive bacteria possess a thick peptidoglycan layer decorated with teichoic acids, whereas Gram-negative bacteria contain a thinner peptidoglycan layer located between the inner and outer membranes, the latter being rich in lipopolysaccharides [1,3]. To combat bacterial infections, antibiotics play a crucial role by damaging bacterial cells through diverse mechanisms, including the destruction of nucleic acids and the cell wall, and the inhibition of protein synthesis [4]. However, excessive use of traditional antibiotics drives bacterial evolution, leading to the emergence of drug-resistant pathogens that undermine the effectiveness of antibiotics in treating pathogenic infections [5]. In addition, bacteria can form a protective layer called a biofilm, a multicellular pathogenic community embedded in a self-produced extracellular polymeric matrix, which provides a physical barrier to antibiotics, preventing their penetration into bacterial cells and leading to severe chronic infections [6,7]. The increasing prevalence of bacterial resistance and the limited efficacy of conventional antibiotics against biofilm-associated infections [8] underscore the urgent need for alternative therapeutic strategies to combat life-threatening pathogenic infections.

Phototheranostics, which combines diagnostics and therapy under light illumination, is a promising alternative to conventional antibacterial therapies due to its non-invasive nature, reduced drug resistance, lower cytotoxicity, and broad-spectrum antimicrobial activity [9–11]. In this regard, fluorescence imaging plays a crucial role by enabling real-time imaging to guide therapeutic decisions [12]. Photodynamic therapy (PDT), which relies on the generation of reactive oxygen species (ROS), initially attracted attention in cancer treatment [13–18]; however, in the 1990s, researchers discovered that it was also highly effective in combating bacterial infections [19]. In PDT, a photosensitizer (PS) is first activated under light irradiation with an appropriate wavelength and excited to the singlet excited state, which then undergoes intersystem crossing to the lowest triplet excited state, where it either directly interacts with the surrounding substances by electron transfer to generate radicals (type I) or interacts with the surrounding oxygen by energy transfer to generate singlet oxygen ($^1O_2$) (type II). The type I mechanism mainly occurs at the bacterial membrane, resulting in lipid peroxidation to generate lipid peroxides, which damage membrane integrity, leading to bacterial death, while $^1O_2$, which is generated through the type II mechanism, is highly toxic and directly interacts with biological macromolecules, including enzymes, nucleic acids, unsaturated lipids, and other cell components, resulting in their oxidation and effective bacterial elimination.

PDT has a fundamental advantage over conventional antibiotics in its ability to eradicate bacteria, regardless of genetic mutations or drug resistance. Unlike antibiotics, which typically act on a single molecular target and thereby impose intense selective pressure that accelerates resistance, PDT relies on the generation of high levels of ROS that indiscriminately oxidize multiple essential cellular components. Upon light activation, ROS simultaneously induce lipid peroxidation of bacterial membranes, protein oxidation, enzyme inactivation, and irreversible nucleic acid damage, ultimately leading to rapid bacterial death. Due to the ultrashort lifetime and limited diffusion distance of ROS, these cytotoxic species act locally and instantaneously, making it extremely challenging for bacteria to develop effective defense mechanisms through mutation or metabolic adaptation. Consequently, even multidrug-resistant or mutated bacteria remain highly susceptible to ROS-mediated photodynamic inactivation, as resistance would require the simultaneous protection of multiple cellular pathways rather than modification of a single drug target [20–22]. In this regard, organic and inorganic PSs have been successfully applied in antimicrobial photodynamic applications. Inorganic PSs, including gold and carbon nanomaterials, copper sulfide, titanium dioxide, and black phosphorus, exhibit high photostability and antimicrobial activity; however, their toxicity and complex metabolism limit their translational potential [23–26]. Similarly, traditional organic PSs with low cytotoxicity, such as cyanine dyes, phenothiazinium salts, and cyclic tetrapyrroles (porphyrins, phthalocyanines, and chlorins), have been successfully applied in antimicrobial PDT [27–30]. However, under physiological aqueous conditions, traditional PSs tend to aggregate, resulting in fluorescence quenching and reduced ROS generation, a phenomenon known as aggregation-caused quenching (ACQ) [31–33]. In contrast to the ACQ effect, which diminishes the emission efficiency of PSs and reduces ROS generation in the aggregated state, aggregation-induced emission luminogens (AIEgens) were first reported in 2001 and have emerged as a superior alternative to traditional PSs owing to their enhanced emission and ROS generation upon aggregation [31]. AIEgens typically have non-planar structures that prevent π–π stacking interactions in the aggregated state, thereby increasing their emission efficiency. In their solution state, they are either non-fluorescent or display weak fluorescence; however, upon aggregation, they emit bright fluorescence due to restricted intramolecular motion [34–36]. Owing to their ease of synthesis, low cytotoxicity, high photostability, and bright fluorescence in the aggregated state, AIEgens have been successfully applied in biomedical fields, including bioimaging [37–39], biosensing [40–42], and phototheranostics [43–45]. In the aggregated state, AIEgens inhibit non-radiative pathways, resulting in high quantum yields and stabilization of the triplet excited state [46,47], thereby enhancing ROS generation for the photodynamic elimination of pathogenic bacteria. Moreover, AIEgens are promising candidates for targeted PDT, as their structures can be easily modified to target specific pathogens. For example, a common strategy for synthesizing AIE-based PSs with broad-spectrum antibacterial activity is to introduce a positive charge to establish strong interactions with negatively charged bacterial surfaces and a hydrophobic tail to interact with the hydrophobic lipid bilayer [48]. Targeted antimicrobial PDT offers a key advantage over non-targeted approaches because ROS have extremely short lifetimes (10–100 ms) and diffusion distances of only ~10 nm [49]. As a result, ROS exert their cytotoxic effects only in the immediate vicinity of the PS. When the PS is selectively delivered, ROS are rapidly consumed at the target site, minimizing diffusion into surrounding tissue. This spatial confinement reduces off-target oxidative damage and protects nearby healthy cells, thereby improving the safety and specificity of PDT [50,51]. Therefore, for effective antimicrobial PDT, a PS should exhibit robust bacterial targeting ability and high ROS-generating capacity.

Despite significant progress in AIE-based antibacterial PSs, many reported systems still rely on conventional fluorophore scaffolds and suffer from limited NIR emission, insufficient membrane specificity, or suboptimal ROS localization, collectively constraining their antibacterial efficacy. Although naphthalimide derivatives have been extensively investigated for biosensing and fluorescence imaging applications [52–56], to the best of our knowledge, no naphthalimide-based AIE PS for broad-spectrum antibacterial PDT has been reported to date. Motivated by this clear gap, here we developed, for the first time, two naphthalimide-based membrane-targeting AIE PSs, TPAPV-NIM-mPy-M and TPAPV-NIM-Py-M, rationally engineered through the integration of cationic pyridinium moieties for bacterial membrane anchoring and a donor–π–acceptor architecture with extended π-conjugation. The PSs were synthesized *via* a Heck cross-coupling strategy using

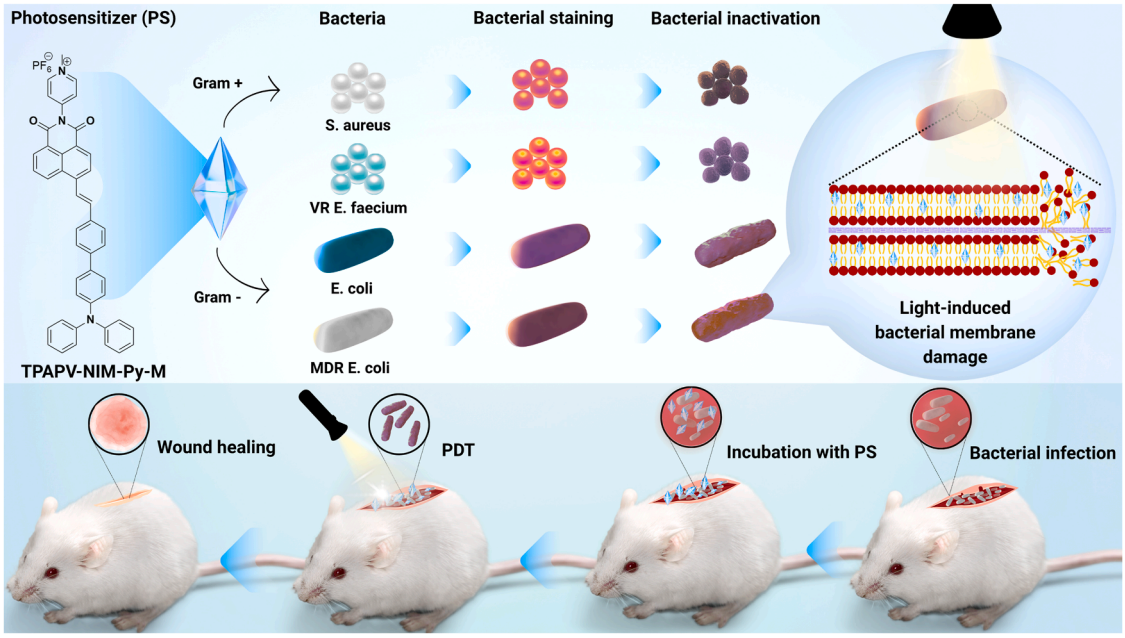

Scheme 1. Schematic illustration of TPAPV-NIM-Py-M. The photosensitizer targets the bacterial membrane, generates reactive oxygen species upon exposure to white light, and promotes enhanced wound-healing ability by eliminating *E. coli* in infected wounds in mice.

triphenylamine (TPA) as an electron-donating unit and naphthalimide as an electron-accepting core, endowing the molecules with pronounced AIE characteristics, NIR emission, and efficient generation of both type I and type II ROS under low-intensity white-light irradiation. Owing to its fully π-conjugated structure and enhanced intramolecular charge transfer, TPAPV-NIM-Py-M exhibited strong ROS generation, demonstrated effective photodynamic eradication of Gram-positive and Gram-negative bacteria, and accelerated wound healing in an *E. coli*–infected model (Scheme 1).

2. Experimental section

2.1. Synthetic procedures

The detailed synthetic procedures for TPAPV-NIM-mPy and TPAPV-NIM-Py are provided in the Supporting Information, and the routes to TPAPV-NIM-mPy-M and TPAPV-NIM-Py-M are shown in Scheme S1. The NMR and MS spectra are presented in Figs. S1–S11.

2.1.1. Synthesis of TPAPV-NIM-mPy-M

TPAPV-NIM-mPy-M was synthesized by reacting 0.150 g (0.237 mmol) of TPAPV-NIM-mPy with excess iodomethane in 10 mL dry acetonitrile at 90 °C for 12 h. After completion of the reaction, as confirmed by thin-layer chromatography (TLC), the acetonitrile was evaporated under vacuum, and the resulting product was taken up in ethyl acetate, filtered, washed with ethyl acetate, and dried under vacuum at 60°C for 2 h. Thereafter, the resulting product was taken up in 5 mL of acetone, without further purification, and treated with a 5 mL aqueous saturated solution of potassium hexafluorophosphate (KPF_6) for 2 h at room temperature, followed by the evaporation of acetone under vacuum. The resulting suspension was vacuum-filtered and washed with DI water to obtain 0.137 g of a red solid (yield: 72.99%), which was dried under vacuum at 60°C overnight. ^{1}H-NMR (DMSO-*d6*, 400 MHz): δ/ppm = 4.29 (s, 3H), 5.49 (d, *J* = 8 Hz, 2H), 7.06 (m, 5H), 7.32 (m, 4H), 7.53 (m, 1H), 7.71 (m, 3H), 7.95 (m, 2H), 8.06 (m, 1H), 8.19 (m, 3H), 8.30 (m, 3H), 8.57 (m, 3H), 8.56 (m, 3H), 9.10 (d, *J* = 8 Hz, 1H). ^{13}C-NMR (DMSO-*d6*, 100 MHz): δ/ppm = 43.16, 47.80, 122.59, 123.23, 123.39, 123.59, 123.87, 124.73, 125.64, 125.72, 126.22, 126.81, 127.55, 128.03, 128.74, 129.02, 129.32, 129.42, 130.11, 130.46, 131.28, 131.66, 131.93, 132.31, 133.45, 135.51, 135.62, 140.33, 145.66, 147.41, 157.09, 157.29, 163.67, 164.18. HRMS (ESI): (m/z) calculated for $C_{45}H_{34}N_3O_2^+$ $[M\text{-}PF_6]^+$ 648.26455, found 648.26588.

2.1.2. Synthesis of TPAPV-NIM-Py-M

TPAPV-NIM-Py-M was synthesized using the same procedure as that described for TPAPV-NIM-mPy-M, except that dry dimethylformamide (DMF) was used instead of acetonitrile; and a dark red solid was obtained (yield: 75.85%). ^{1}H-NMR (DMSO-*d6*, 400 MHz): δ/ppm = 4.45 (s, 3H), 7.08 (m, 8H), 7.35 (m, 4H), 7.73 (m, 5H), 7.99 (m, 3H), 8.34 (m, 4H), 8.57 (d, *J* = 8 Hz, 1H), 8.63 (d, *J* = 8 Hz, 1H), 9.19 (t, *J* = 8 Hz, 3H). ^{13}C-NMR (DMSO-*d6*, 100 MHz): δ/ppm = 67.41, 120.83, 122.71, 123.17, 123.58, 123.86, 123.99, 124.75, 126.85, 127.64, 128.04, 128.80, 129.13, 129.19, 129.71, 130.10, 131.51, 131.83, 132.35, 133.58, 135.62, 135.91, 140.41, 142.50, 147.43, 147.47, 151.39, 163.11, 163.44. HRMS (ESI): (m/z) calculated for $C_{44}H_{32}N_3O_2^+$ $[M\text{-}PF_6]^+$ 634.24890, found 634.25031.

2.2. Detection of reactive oxygen species (ROS)

2.2.1. Detection of superoxide anions ($O_2^{\bullet-}$)

The ability of the synthesized PSs to generate superoxide anions ($O_2^{\bullet-}$) was evaluated using dihydrorhodamine 123 (DHR-123), a commercially available standard sensor for $O_2^{\bullet-}$ detection. In detail, 1 mM solutions of the synthesized PSs and DHR-123 in dimethyl sulfoxide were diluted to 5 μM in deionized (DI) water. Then, they were mixed in a 1:1 ratio to obtain final working solutions of 2.5 μM for the synthesized PSs and DHR-123. The mixtures were irradiated with white light (27 mW/cm^2) for 0–80 sec, and changes in fluorescence intensity at 527 nm were monitored using a fluorescence spectrophotometer.

2.2.2. Detection of hydroxyl radicals ($OH^{\bullet}$)

The ability of the synthesized PSs to generate hydroxyl radicals ($OH^{\bullet}$) was evaluated using hydroxyphenyl fluorescein (HPF), a commercially available standard sensor for $OH^{\bullet}$ detection. In detail, 1 mM solutions of the synthesized PSs and HPF in dimethyl sulfoxide were separately diluted to 10 μM in DI water, then mixed in a 1:1 ratio to obtain final working solutions of 5 μM concentrations for the

synthesized PSs and HPF. The mixtures were irradiated with white light (27 mW/cm^2) for 1–4 min, and changes in fluorescence intensity at 515 nm were monitored using a fluorescence spectrophotometer.

2.2.3. Detection of singlet oxygen

The ability of the synthesized PSs to generate singlet oxygen was evaluated using 9,10-Anthracenediyl-bis(methylene)dimalonic acid (ABDA), a commercially available standard indicator for $^1O_2$ detection. In detail, 1 mM solutions of the synthesized PSs and ABDA in dimethyl sulfoxide were diluted to 10 μM and 150 μM in DI water, respectively, and then mixed in a 1:1 ratio to obtain final working solutions of 5 μM and 75 μM concentrations for PSs and ABDA, respectively. The mixtures were irradiated with white light (27 mW/cm^2) for 10–90 sec, and the decomposition of ABDA at 400 nm was recorded using a UV-visible spectrophotometer. To assess the effectiveness of the synthesized PSs, the commercial PSs chlorin e6 (Ce6, 5 μM working concentration) and Rose Bengal (5 μM working concentration) were also used, following the procedures for TPAPV-NIM-mPy-M and TPAPV-NIM-Py-M. The decomposition of ABDA was monitored at 400 nm using a UV-visible spectrophotometer.

2.2.4. Total ROS detection in bacterial cells (Intracellular ROS generation)

The intracellular ROS-generating ability of the synthesized PSs was evaluated using 2′,7′-dichlorodihydrofluorescein diacetate (DCFH-DA), a standard commercial indicator for detecting intracellular ROS. In detail, bacterial suspensions of *S. aureus* and *E. coli* with an $OD_{600} = 0.1$ were separately incubated with 5 μM solutions of the synthesized PSs in phosphate-buffered saline (PBS) at 37°C under shaking (200 rpm) for 30 min. Thereafter, the cells were washed with PBS to remove excess PSs, treated with 20 μM DCFH-DA, incubated for a further 30 min at 37°C under shaking conditions, then washed with PBS, irradiated with light (40 mW/cm^2) for 15 min, and immediately observed under a confocal microscope.

2.3. Cytotoxicity evaluation

The cytotoxicity of the synthesized PSs was evaluated against HUVECs and WI-38 cells. To assess biocompatibility, HUVECs and WI-38 cells were cultured in Dulbecco's Modified Eagle Medium (DMEM) for 24 h. Thereafter, the cells were separately seeded in 96-well plates (5×10^3 cells per well) for an additional 24 h, then treated with different concentrations (0, 5, 10, 20, 30, 40, and 50 μM) of the synthesized PSs, followed by a further 24 h of incubation. After that, cell viability was evaluated using a standard MTT assay: each well was treated with 10 μL of MTT solution in PBS (5 mg/mL) and incubated at 37°C for 4 h. Then, the medium containing unreacted MTT was discarded, each well was treated with 150 μL of DMSO to dissolve the formazan crystals, and the plate was shaken for an additional 5 min. Cytotoxicity was evaluated using a multi-mode plate reader (Biotek, HTX S1 LFA, USA) by measuring absorbance at 570 nm with 640 nm as the reference wavelength, and cell viability was calculated using the following formula.

$$\text{Cellviability}(\%) = \left[\left(OD_{Sample} - \right.\right. \\ \left.\left. - OD_{Blank}\right) / \left(OD_{Control} - - OD_{Blank}\right)\right] \times 100$$

2.4. Laser scanning confocal fluorescence imaging

To perform the bacterial imaging experiments, *S. aureus* and *E. coli* ($OD_{600} = 0.1$) were separately incubated with TPAPV-NIM-mPy-M and TPAPV-NIM-Py-M (5 μM) at 37°C under shaking (200 rpm) for 30 min. Next, the bacteria were centrifuged at 10,000 rpm for 5 min, washed with PBS, and treated with DAPI (20 μM) for 10 min at 37 °C under shaking conditions (200 rpm), followed by PBS washing. For confocal imaging, 20 μL of the stained bacterial suspension was dropped onto a glass slide, a coverslip was applied, and the sample was observed using a confocal laser-scanning microscope with a 63 × oil-immersion objective. The confocal fluorescence images were acquired using excitation with a 488 nm laser for TPAPV-NIM-mPy-M and TPAPV-NIM-Py-M, while a 405 nm laser was used for DAPI.

2.5. Live/dead cell staining

Bacterial suspensions (*S. aureus* and *E. coli*) with an $OD_{600} = 0.1$ were separately incubated with 10 μM solutions of the synthesized PSs in PBS at 37°C under shaking (200 rpm) for 30 min. Thereafter, the cells were washed with PBS to remove excess PSs and irradiated with white light (40 mW/cm^2) for 30 min. Then, the bacterial suspensions were treated with 5 μM calcein-AM and 15 μM propidium iodide (PI) and incubated for an additional 30 min at 37°C with shaking. After that, the cells were washed with PBS to remove excess dye, fixed onto a glass slide, and observed under a confocal microscope promptly. For the control groups, bacterial cells not treated with the synthesized PSs were irradiated with white light (40 mW/cm^2), then stained with calcein-AM and PI and observed under a confocal microscope immediately.

2.6. In vitro antibacterial photodynamic therapy

Bacterial suspensions of *S. aureus, E. coli*, VR *E. faecium*, and MDR *E. coli* were adjusted to an OD_{600} of 0.1 and incubated with the PSs in PBS at 37°C under shaking conditions (200 rpm) for 30 min. For *S. aureus* and *E. coli*, TPAPV-NIM-mPy-M and TPAPV-NIM-Py-M were tested at 2.5, 5, 7.5, and 10 μM, whereas TPAPV-NIM-Py-M was tested at 10 μM against VR *E. faecium* and MDR *E. coli*. The bacteria were then washed with PBS to remove unbound PSs and divided into dark and light groups. The light groups were exposed to white light at 40 mW/cm^2 for 30 min, while the dark groups were treated identically without irradiation. Light-only controls were prepared using bacterial suspensions without PSs. Following treatment, all samples were serially diluted to 1×10^4 CFU/mL, and 70 μL of each suspension was spread onto LB-agar plates. After incubation at 37°C for 24 h, the colonies were counted to evaluate antibacterial efficacy.

2.7. Antibiofilm assay

Bacterial suspensions (*S. aureus* and *E. coli*) with an $OD_{600} = 0.1$ were added to 6-well plates and incubated at 37°C for 36 h in LB medium. After the formation of biofilms, the LB medium was discarded, and biofilms were treated with PBS and classified into three categories: blank (biofilms only), dark group (biofilms treated with synthesized PSs under dark conditions), and light group (biofilms treated with the synthesized PSs under PDT conditions). The dark and light groups were treated with the synthesized PSs (50 μM) and incubated for 4 h. Thereafter, the light groups were exposed to white light (85 mW/cm^2) for 40 min. Afterward, LB medium was discarded from all groups, and the biofilms were washed twice with PBS and fixed with methanol for 15 min. Methanol was removed, and the biofilms were air-dried for 30 min, followed by staining with 0.1% (w/v) crystal violet for 15 min. Then, the biofilms were washed twice with PBS to remove the excess dye, and the remaining dye was dissolved by adding a sufficient amount of 30% acetic acid, followed by shaking for 5 min. The obtained solutions were diluted 20-fold, photographed, and quantified by measuring the absorbance at 595 nm using a microplate reader.

2.8. Bacterial surface observation

Bacterial suspensions (*S. aureus* and *E. coli*) with an $OD_{600} = 0.2$ were separately incubated with 10 μM of the synthesized PSs in PBS at 37°C under shaking (200 rpm) for 30 min. Thereafter, the cells were washed with PBS to remove excess PSs and divided into two groups (dark and light). The light groups were irradiated with white light (40 mW/cm^2) for 30 min, and the bacterial suspensions were dropped onto a clean 1 × 1 cm^2 glass slide in a 24-well plate, treated with 2.5% glutaraldehyde in

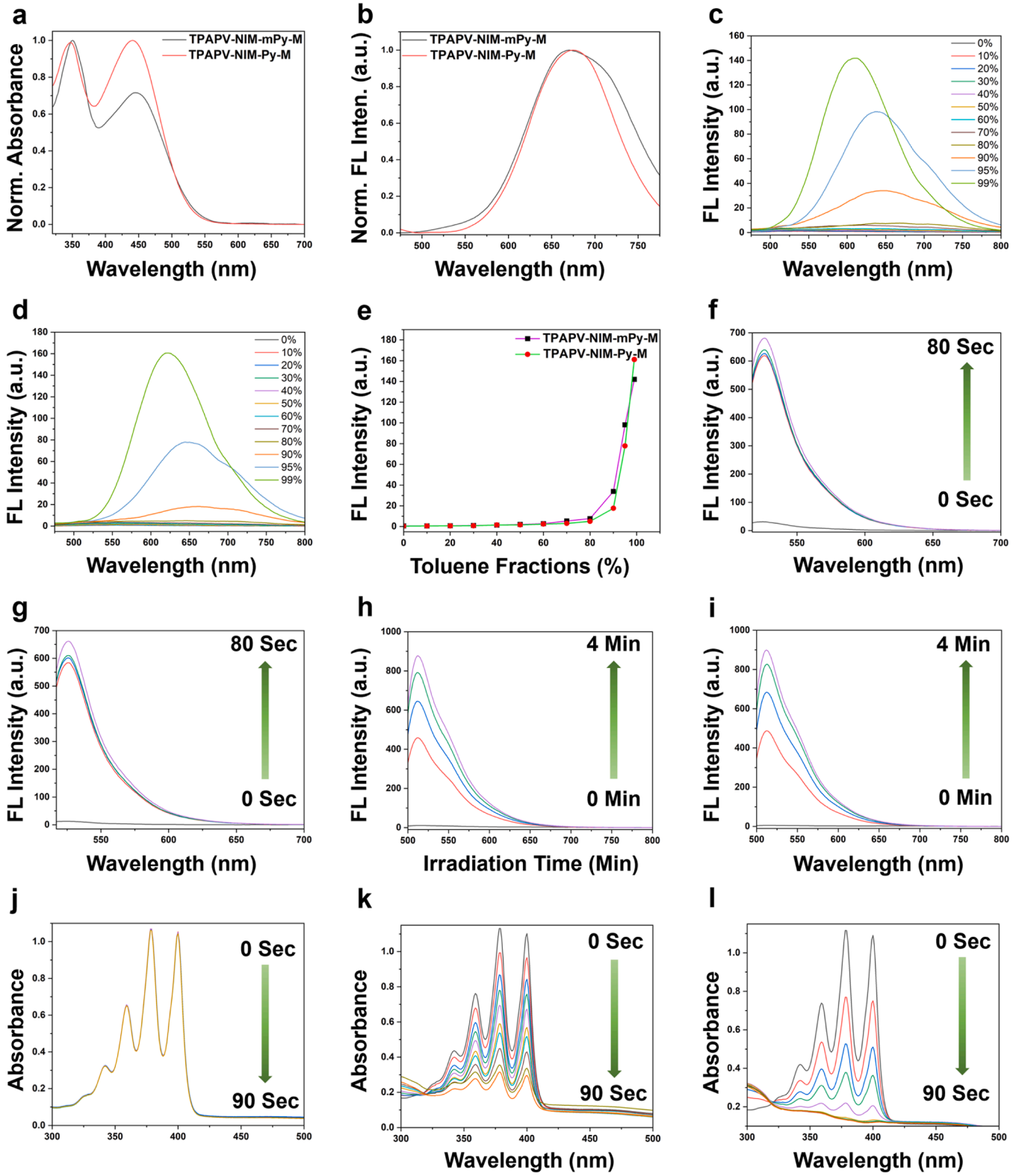

Fig. 1. a) Absorption spectra of TPAPV-NIM-mPy-M and TPAPV-NIM-Py-M in chloroform. b) Fluorescence emission spectra of TPAPV-NIM-mPy-M and TPAPV-NIM-Py-M in chloroform. c) Fluorescence emission spectra of TPAPV-NIM-mPy-M in DMSO/toluene mixtures with different toluene fractions based on volume. d) Fluorescence emission spectra of TPAPV-NIM-Py-M in DMSO/toluene mixtures with different toluene fractions based on volume. e) Plots of the changes in the fluorescence intensities of TPAPV-NIM-mPy-M and TPAPV-NIM-Py-M with varying fractions of toluene. f) Changes in the intensities of fluorescence emission spectra of DHR-123 (2.5 μM) under white-light irradiation in the presence of TPAPV-NIM-mPy-M (2.5 μM). g) Changes in the intensities of fluorescence emission spectra of DHR-123 (2.5 μM) under white-light irradiation in the presence of TPAPV-NIM-Py-M (2.5 μM). h) Changes in the intensities of fluorescence emission spectra of HPF (5 μM) under white-light irradiation in the presence of TPAPV-NIM-mPy-M (5 μM). i) Changes in the intensities of fluorescence emission spectra of HPF (5 μM) under white-light irradiation in the presence of TPAPV-NIM-Py-M (5 μM). j) Absorption spectra of ABDA (75 μM) under white-light irradiation. k) Absorption spectra of ABDA in the presence of TPAPV-NIM-mPy-M (5 μM). l) Absorption spectra of ABDA in the presence of TPAPV-NIM-Py-M (5 μM).

PBS to fix the bacteria to the glass surface, and stored at 4 °C overnight. The same protocol was followed for the dark and bacteria-alone groups, except that white-light irradiation was omitted. Thereafter, the bacteria were dehydrated in absolute ethanol (30%, 40%, 50%, 60%, 70%, 80%, 90%, and 100%) for 15 min and then observed under a scanning electron microscope after gold coating.

2.9. Zeta potential measurement

Bacterial suspensions (*S. aureus* and *E. coli*) with an $OD_{600} = 0.1$ were separately incubated with 5 μM of the synthesized PSs in PBS at 37°C under shaking (200 rpm) for 30 min. After that, the cells were washed with PBS to remove excess PSs, and the zeta potential was measured *via* a Zetasizer (Malvern). The zeta potential of bacteria alone (*S. aureus* and *E. coli*) with an OD_{600} of 0.1 was also measured as a control. To measure the zeta potential of TPAPV-NIM-mPy-M and TPAPV-NIM-Py-M, a 1 mM solution of TPAPV-NIM-mPy-M or TPAPV-NIM-Py-M in DMSO was diluted to 5 μM in DI water, and the zeta potential was measured using a Zetasizer (Malvern).

2.10. In vivo wound healing experiment

BALB/c mice (~6 weeks) were obtained from the animal center of Erciyes University, and the wound-healing experiment was performed at the same animal facility of Erciyes University. The animal experiment was performed in accordance with the approved protocol of the Erciyes University Ethics Committee (No: 24/216). To assess the wound-healing efficacy of TPAPV-NIM-Py-M, a deep incision (~20 mm in length) was performed on the dorsal region of each mouse. After that, the mice were divided into four groups with three mice in each group: (1) dark group (*E. coli* + TPAPV-NIM-Py-M), (2) PBS group (*E. coli* + PBS + light), (3) *E. coli* group (*E. coli* only), and (4) light group (*E. coli* + TPAPV-NIM-Py-M + light). At 24 h post-infection with *E. coli*, groups (1) and (4) were administered 20 μM TPAPV-NIM-Py-M by injection into the wounds and kept at room temperature for 3 h, whereas group (2) received PBS alone. After 3 h, the PBS and light groups were exposed to white light (~85 mW/cm^2) for 30 min, and the wound-healing process was tracked photographically throughout the PDT experiment.

2.11. Blood hemolysis experiment

Fresh blood (1 mL) was collected from a healthy BALB/c mouse, centrifuged at 10,000 rpm for 10 min at 4°C to isolate red blood cells (RBCs), and the collected RBCs were washed twice with PBS. Afterward, the RBCs were collected in PBS (8 mL) and vortexed to obtain a fine RBC suspension. To evaluate the hemolytic effect of the synthesized PSs, DI water was used as a positive control, and PBS was used as a negative control. To perform the hemolysis experiment, 100 μL of RBC suspension was added to 400 μL of PBS to obtain a final concentration of 2.5 μM for the synthesized PSs, and for other working concentrations (5 μM, 10 μM, 20 μM, 30 μM, and 50 μM) of TPAPV-NIM-mPy-M and TPAPV-NIM-Py-M, a similar protocol was adopted. For the control groups, 100 μL of RBC suspension was either added to 400 μL of PBS or DI water. Thereafter, the samples were incubated at 37 °C for 2 h. The hemolytic effect of the synthesized PSs was recorded at 577 nm using a microplate reader, and the percentage hemolysis was calculated using the following formula:

$$\text{Hemolysis}(\%) = \left[\left(A_{\text{sample}} - - A_{\text{NegativeControl}}\right) / \left(A_{\text{PositiveControl}} - - A_{\text{NegativeControl}}\right)\right] \times 100$$

where A denotes the absorbance at 577 nm.

2.12. Hematoxylin and eosin (H&E) staining

After 9 days of the wound-healing experiment, vital organs, including the heart, liver, lungs, spleen, and kidneys, were collected from the different BALB/c mouse treatment groups (light, PBS, *E. coli* only, and dark), and stored in 10% formaldehyde solution at 4 °C. For hematoxylin and eosin (H&E) staining, the tissues were dehydrated through a graded series of alcohols, then cleared in xylene, and embedded in paraffin blocks. After that, five-micrometer-thick sections were cut with a microtome, stained with Hematoxylin and Eosin (H&E), and observed under a light microscope using an LED light source.

2.13. Statistical analysis

Quantitative data are expressed as the mean ± standard deviation (SD), with the number of independent replicates indicated in the corresponding figure legends or experimental sections. Statistical comparisons were performed using Student's *t*-test. A probability value of $p < 0.05$ was considered statistically significant. The number of stars/asterisks indicates the level of statistical significance as follows: ns, not significant; one star/asterisk (*) indicates $p < 0.05$, two stars/asterisks (**) indicate $p < 0.01$, three stars/asterisks (***) indicate $p < 0.001$, and four stars/asterisks (****) indicate $p < 0.0001$.

3. Results and discussion

3.1. Molecular design and photophysical properties

Introducing donor–acceptor character into a molecule is a promising strategy for obtaining fluorescent molecules with red-shifted absorption and emission wavelengths, which is beneficial for deep-tissue penetration in bioimaging and PDT [57]. In addition, such a push-pull effect in a molecule significantly enhances intramolecular charge transfer (ICT), thereby enhancing the molecule's ROS-generating ability by effectively separating the highest occupied molecular orbital (HOMO) from the lowest unoccupied molecular orbital (LUMO), facilitating the intersystem crossing by reducing the energy gap (ΔE_{ST}) between singlet (S_1) and triplet (T_1) states [58,59]. Given the widespread applications of D–A-type molecules in fluorescence imaging and phototheranostics, herein, we report the synthesis and application of two novel naphthalimide-based PSs designated TPAPV-NIM-mPy-M and TPAPV-NIM-Py-M, for fluorescence imaging and the photodynamic elimination of Gram-positive and Gram-negative bacterial strains. These molecules were synthesized by Heck cross-coupling and the Menshutkin reaction (Scheme S1), and their molecular structures were characterized by nuclear magnetic resonance spectroscopy and high-resolution mass spectrometry (Figs. S1–S11). To synthesize TPAPV-NIM-mPy-M and TPAPV-NIM-Py-M, the naphthalimide (NIM) core was chosen as the electron-withdrawing moiety, and triphenylamine (TPA) was chosen as the electron-donating segment. To effectively separate the HOMO and LUMO orbitals, a π-bridge was introduced between the donor and acceptor moieties, as D–π–A molecular engineering is a promising strategy for effective HOMO-LUMO separation and high ROS generation [60]. To establish strong interactions with the negatively charged surfaces of pathogens, TPAPV-NIM-mPy-M and TPAPV-NIM-Py-M were further functionalized with pyridinium moieties at the terminal positions, thereby enhancing the D-A strength of the molecules owing to their electron-deficient nature [57]. In addition to its electron-donating ability, TPA can also enhance the fluorescence of TPAPV-NIM-mPy-M and TPAPV-NIM-Py-M in the aggregated or solid states by sterically hindering π–π stacking due to the its twisted molecular structure [61].

The absorption properties of the synthesized molecules were studied in chloroform using UV-visible spectroscopy, and the results indicate that both PSs exhibit broad absorption from 350–550 nm, with maximum absorption in the visible region at 447 nm and 441 nm for TPAPV-NIM-mPy-M and TPAPV-NIM-Py-M, respectively (Fig. 1a). The fluorescence emission of the PSs was evaluated in chloroform *via* fluorescence spectroscopy, where both PSs displayed broad emission from 500 nm to the NIR-I region (beyond 700 nm) with maximum emission at

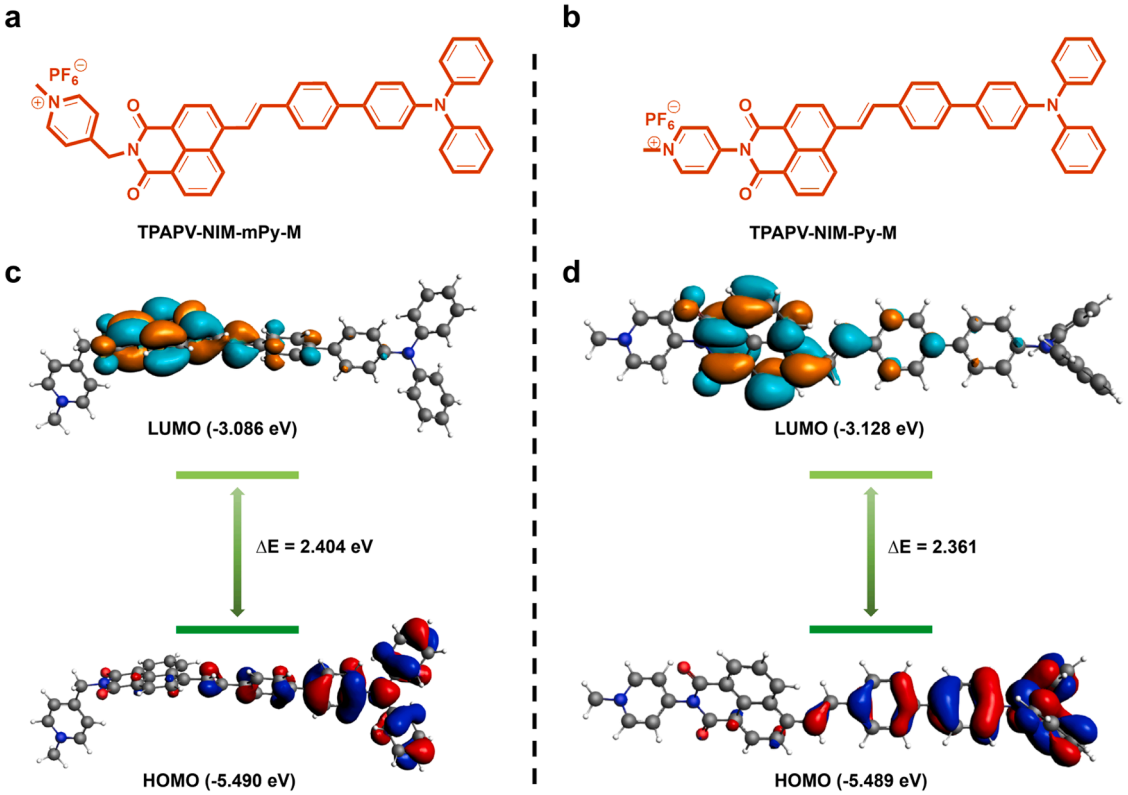

Fig. 2. a) Chemical structure of TPAPV-NIM-mPy-M, b) Chemical structure of TPAPV-NIM-Py-M, c) HOMO and LUMO orbitals of TPAPV-NIM-mPy-M, and d) HOMO and LUMO orbitals of TPAPV-NIM-Py-M.

670 nm and 677 nm for TPAPV-NIM-mPy-M and TPAPV-NIM-Py-M, respectively (Fig. 1b). The Stokes shifts for TPAPV-NIM-mPy-M and TPAPV-NIM-Py-M were calculated to be 223 and 236 nm, respectively, which are ideal for fluorescent molecules used in biomedical applications to mitigate fluorophore self-quenching in the solid/aggregated state. TPAPV-NIM-mPy-M and TPAPV-NIM-Py-M, functionalized with TPA, were expected to exhibit AIE characteristics owing to the twisted molecular structure of TPA, which resists π–π stacking through steric hindrance. To validate our hypothesis, various ratios of dimethyl sulfoxide (DMSO) to toluene were used to investigate the AIE properties of the synthesized PSs. In pure DMSO, the PSs did not show fluorescence, attributed to the TICT (twisted intramolecular charge-transfer) effect in a polar medium. As the toluene fraction increased, fluorescence increased and reached a maximum at 99% toluene for both AIEgens, with a slight blue shift attributed to the TICT effect in a less polar mixture (Fig. 1c-d). These results suggest that both TPAPV-NIM-mPy-M and TPAPV-NIM-Py-M, with twisted molecular structures, display AIE characteristics and are suitable candidates for bioimaging applications.

3.2. *Light-triggered ROS generation*

Encouraged by the strong AIE characteristics of the synthesized AIEgens, we further evaluated their ROS-generating ability under white-light irradiation using dihydrorhodamine 123 (DHR-123), hydroxyphenyl fluorescein (HPF), and ABDA, which serve as commercial indicators for the detection of superoxide anions ($O_2^{\bullet-}$), hydroxyl radicals ($OH^{\bullet}$), and singlet oxygen ($^1O_2$), respectively. Superoxide anions were detected in an aqueous medium by separately mixing 5 μM solutions of TPAPV-NIM-mPy-M and TPAPV-NIM-Py-M with a 5 μM solution of DHR-123 in a 1:1 volume ratio to obtain a 2.5 μM final working solution of each. The mixtures were irradiated with white light (27 mW/cm^2) from 0 to 80 sec, and changes in the fluorescence intensity at 527 nm were recorded using a fluorescence spectrophotometer. The fluorescence intensity at 527 nm increased sharply with irradiation time, indicating the generation of superoxide anions under white-light irradiation (Fig. 1f-g and Fig. S12). Similarly, hydroxyl radicals ($OH^{\bullet}$) were also detected in an aqueous medium by separately mixing 10 μM solutions of TPAPV-NIM-mPy-M and TPAPV-NIM-Py-M with a 10 μM solution of HPF in a 1:1 volume ratio to obtain a 5 μM final working solution of each. The mixtures were irradiated with white light (27 mW/cm^2) from 1 to 4 min, and changes in the fluorescence intensity at 515 nm were recorded using a fluorescence spectrophotometer. The fluorescence intensity at 515 nm increased with irradiation time, indicating the generation of hydroxyl radicals ($OH^{\bullet}$) under white-light irradiation (Fig. 1h-i and Fig. S13).

Next, type II ROS detection was performed in an aqueous medium using ABDA, a standard sensor for singlet oxygen ($^1O_2$). Before the experiment, the photostability of ABDA (75 μM) was evaluated under white-light irradiation (27 mW/cm^2) from 0 to 90 sec, and the rate of ABDA decomposition was monitored from 350 to 400 nm; no decrease in the absorption of ABDA at 350-400 nm was observed (Fig. 1j), strongly supporting its high photostability under white-light irradiation. Thereafter, the singlet oxygen-generating ability of the synthesized AIEgens was assessed by separately mixing a 150 μM aqueous solution of ABDA with 10 μM aqueous solutions of TPAPV-NIM-mPy-M and TPAPV-NIM-Py-M in a 1:1 volume ratio to obtain final working concentrations of 75 μM and 5 μM for ABDA and the AIEgens, respectively, and the absorption of ABDA was recorded at 400 nm. With increasing light irradiation from 0 to 90 sec, the absorption of ABDA at 400 nm gradually decreased, indicating the generation of singlet oxygen under white-light irradiation (Fig. 1k-l). To further evaluate the efficacy of the synthesized AIEgens in singlet oxygen generation, the decomposition of ABDA in the presence of two commercially available PSs, Ce6 and RB, was also evaluated under white-light irradiation from 0 to 90 sec, and the decomposition of ABDA was recorded at 400 nm (Figs. S14 and S15). A comparative analysis of $^1O_2$ generation by the commercial and synthesized PSs showed that

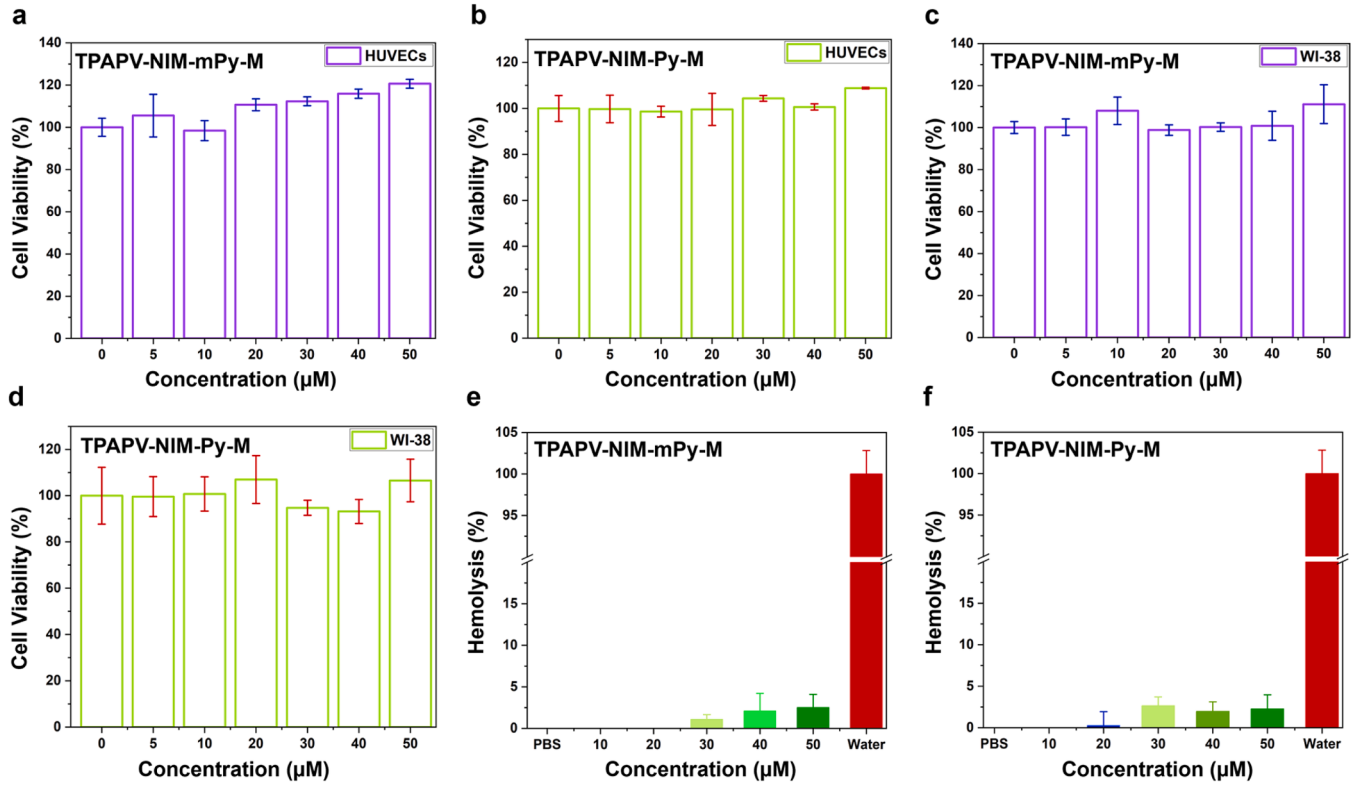

Fig. 3. Cell viability of HUVEC cells treated with different concentrations of a) TPAPV-NIM-mPy-M and b) TPAPV-NIM-Py-M under dark conditions. Cell viability of WI-38 cells treated with different concentrations of: c) TPAPV-NIM-mPy-M and d) TPAPV-NIM-Py-M under dark conditions. Hemolysis rates of the red blood cells treated with varying concentrations of: e) TPAPV-NIM-mPy-M and f) TPAPV-NIM-Py-M.

ABDA consumption reached 90%, 80%, 40%, and 30% after 90 sec of white-light irradiation in the presence of TPAPV-NIM-Py-M, TPAPV-NIM-mPy-M, RB, and Ce6, respectively (Fig. S16), indicating the superior ROS-generating ability of the synthesized PSs compared with commercially available RB and Ce6. These results indicate that TPAPV-NIM-Py-M, with greater type I and type II ROS-generating capacity, is a suitable candidate for PDT. The concurrent generation of type I and type II ROS is particularly advantageous in hypoxic or oxygen-limited infection environments, where traditional type II PDT is less effective, thereby enhancing the robustness and applicability of the proposed PS for antibacterial therapy.

The enhanced ROS-generating ability of TPAPV-NIM-Py-M was further supported by theoretical calculations at the B3LYP/DZP level of theory using ADF 2023. The chemical structures and HOMO and LUMO energy levels of TPAPV-NIM-mPy-M and TPAPV-NIM-Py-M are presented in Fig. 2a-d, while the excited-state energetics are presented in Fig. S17. The detailed excited-state properties are summarized in Tables S1 and S2. In the TPAPV-NIM-mPy-M structure, the pyridinium moiety acts as an electron acceptor but is electronically decoupled from the rest of the molecule by an intervening –CH_2–σ-bond, which disrupts π-conjugation. In contrast, in TPAPV-NIM-Py-M, the pyridinium unit is directly bonded to the conjugated framework, enabling stronger electronic coupling and more effective delocalization. As a consequence, TPAPV-NIM-Py-M exhibits a slight red shift in the low-lying excited states along with a reduced singlet–triplet energy gap relative to TPAPV-NIM-mPy-M. Furthermore, the direct conjugation in TPAPV-NIM-Py-M enhances charge-transfer character, which may be further modulated by vibronic effects associated with the dihedral angle between the pyridinium group and the molecular backbone. These effects are expected to facilitate intersystem crossing and may contribute to the enhanced ROS generation in the TPAPV-NIM-Py-M system.

3.3. Cytotoxicity and blood hemolysis

Before evaluating the biomedical applications of TPAPV-NIM-mPy-M and TPAPV-NIM-Py-M, we assessed the biosafety of the synthesized PSs using MTT and hemolysis assays. To evaluate the cytotoxicity, HUVECs and WI-38 cells were separately incubated with different concentrations (0–50 μM) of TPAPV-NIM-mPy-M and TPAPV-NIM-Py-M for 24 h at 37 °C. Next, the cells were washed with PBS to remove excess PSs, and cell viability was measured using a standard MTT assay in a microplate reader. Cell viability remained comparable to the control group across all tested conditions, even at high concentrations, indicating good biocompatibility of the synthesized PSs (Fig. 3a-d). To further evaluate the biosafety profile of the synthesized PSs, the hemolytic effect of TPAPV-NIM-mPy-M and TPAPV-NIM-Py-M on red blood cells (RBCs) collected from a healthy BALB/c mouse was investigated. To measure the hemolytic effect, RBC suspensions were incubated with different concentrations (0–50 μM) of TPAPV-NIM-mPy-M and TPAPV-NIM-Py-M at 37 °C for 2 h. For comparison, RBC suspensions were also incubated with DI water (positive control) and PBS (negative control), and the hemolytic effect was measured using a microplate reader. Neither PS showed an apparent hemolytic effect even at the highest concentration (50 μM) (Fig. 3e-f), further confirming the high biosafety of TPAPV-NIM-mPy-M and TPAPV-NIM-Py-M, thereby making them promising candidates for further translational development.

3.4. Bacterial imaging

Encouraged by the strong fluorescence in the aggregated state, higher type I and II ROS generation in aqueous media, and a favorable biosafety profile, we further evaluated the synthesized PSs for fluorescence imaging of Gram-positive and Gram-negative bacteria *via* confocal laser scanning microscopy, because fluorescence imaging technique is non-invasive and plays a key role in the visualization of cellular

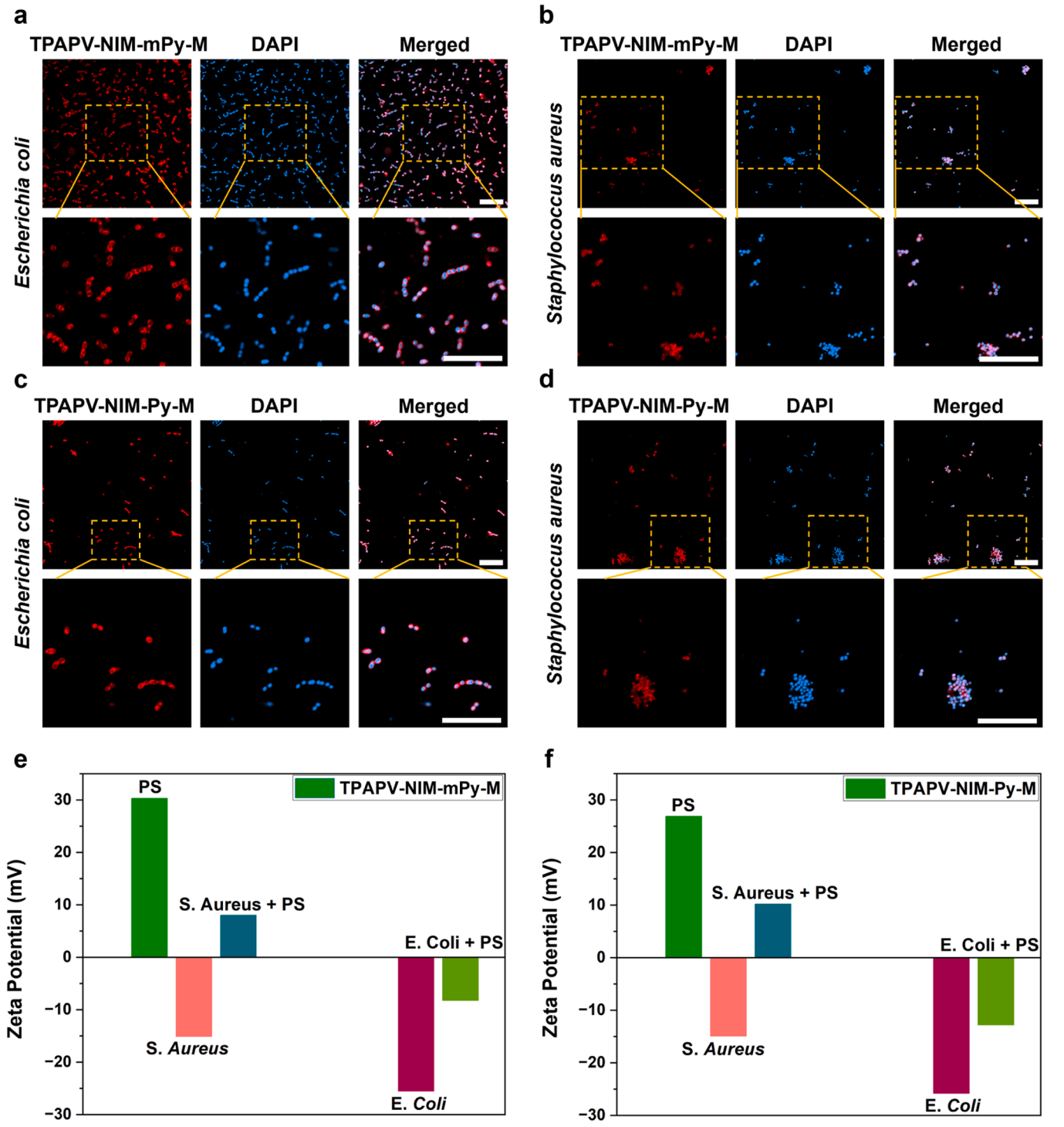

Fig. 4. a) Confocal fluorescence images of *E. coli* treated with TPAPV-NIM-mPy-M (red fluorescence signals), DAPI (blue fluorescence signals), and merged images. b) Confocal fluorescence images of *S. aureus* treated with TPAPV-NIM-mPy-M (red fluorescence signals), DAPI (blue fluorescence signals), and merged images. c) Confocal fluorescence images of *E. coli* treated with TPAPV-NIM-Py-M (red fluorescence signals), DAPI (blue fluorescence signals), and merged images. d) Confocal fluorescence images of *S. aureus* treated with TPAPV-NIM-Py-M (red fluorescence signals), DAPI (blue fluorescence signals), and merged images. Note: The dotted area in each image (a-d) represents the zoomed area. Concentrations of TPAPV-NIM-mPy-M and TPAPV-NIM-Py-M: 5 μM and DAPI: 20 μM. TPAPV-NIM-mPy-M and TPAPV-NIM-Py-M were excited with a 488 nm laser, and the emission was collected between 610 and 700 nm. DAPI was excited with a 405 nm laser, and the emission was collected between 400 and 560 nm. Scale bars: 5 μm and 2 μm (for zoomed images). e) Zeta potential values of TPAPV-NIM-mPy-M alone, *S. aureus,* and *E. coli* with or without the treatment of TPAPV-NIM-mPy-M. f) Zeta potential values of TPAPV-NIM-Py-M alone, *S. aureus,* and *E. coli* with or without the treatment of TPAPV-NIM-Py-M.

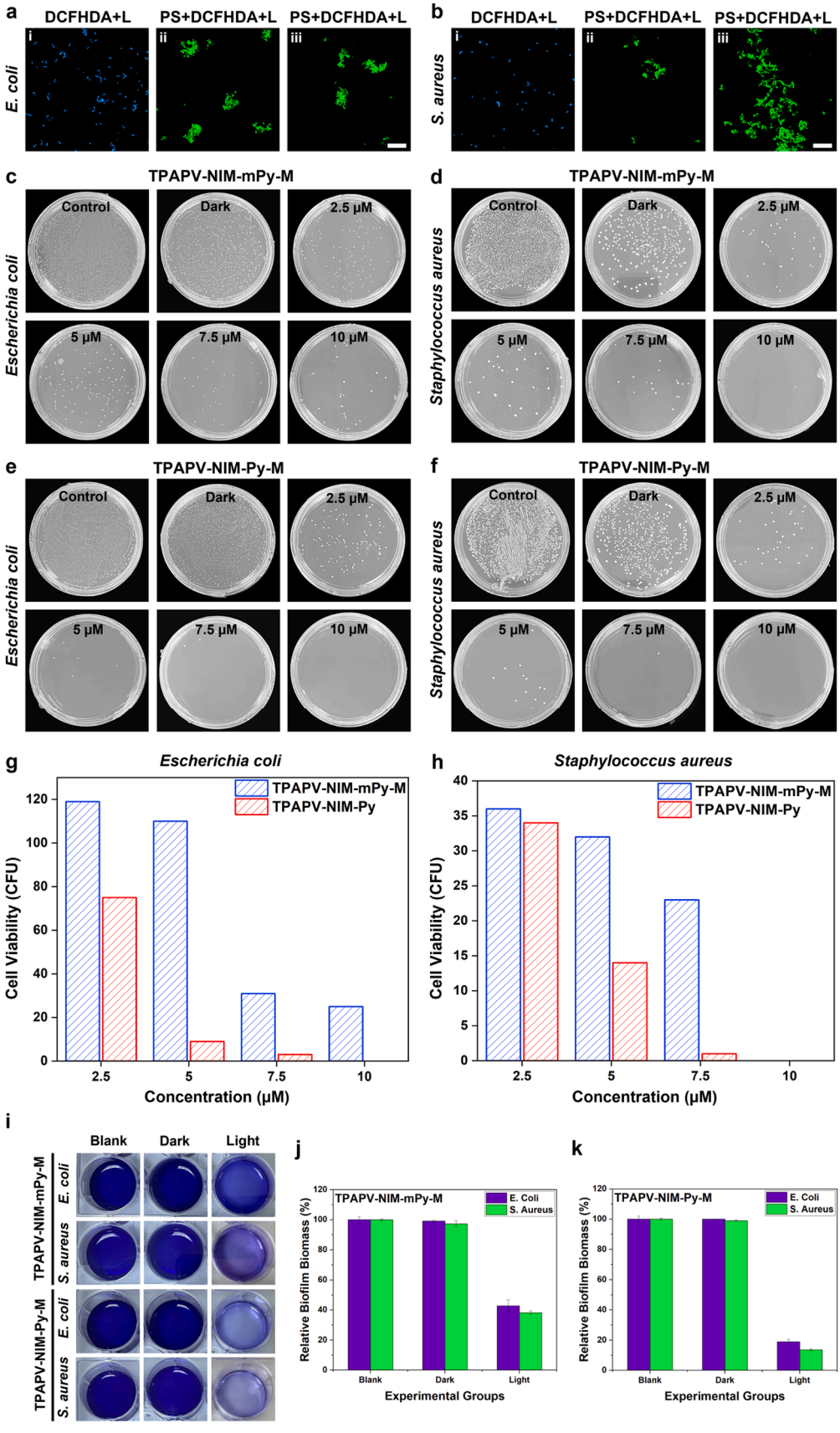

(caption on next page)

Fig. 5. Detection of intracellular ROS *via* DCFH-DA (20 μM) in bacterial cells: a-i) *E. coli* incubated with DAPI and DCFH-DA + light irradiation, a-ii) *E. coli* incubated with TPAPV-NIM-mPy-M and DCFH-DA + light irradiation, and a-iii) *E. coli* incubated with TPAPV-NIM-Py-M and DCFH-DA + light irradiation. b-i) *S. aureus* incubated with DAPI and DCFH-DA + light irradiation, b-ii) *S. aureus* incubated with TPAPV-NIM-mPy-M and DCFH-DA + light irradiation, and b-iii) *S. aureus* incubated with TPAPV-NIM-Py-M and DCFH-DA + light irradiation. Scale bar: 5 μm. c) Survival rates of *E. coli* under different treatments: control (*E. coli* only + light), dark (*E. coli* treated with TPAPV-NIM-mPy-M (10 μM) under dark conditions), and light (*E. coli* treated with TPAPV-NIM-mPy-M (2.5-10 μM) under light irradiation). d) Survival rates of *S. aureus* under different treatments: control (*S. aureus* only + light), dark (*S. aureus* treated with TPAPV-NIM-mPy-M (10 μM) under dark conditions), and light (*S. aureus* treated with TPAPV-NIM-mPy-M (2.5-10 μM) under light irradiation). e) Survival rates of *E. coli* under different treatments: control (*E. coli* only + light), dark (*E. coli* treated with TPAPV-NIM-Py-M (10 μM) under dark conditions), and light (*E. coli* treated with TPAPV-NIM-Py-M (2.5-10 μM) under light irradiation). f) Survival rates of *S. aureus* under different treatments: control (*S. aureus* only + light), dark (*S. aureus* treated with TPAPV-NIM-Py-M (10 μM) under dark conditions), and light (*S. aureus* treated with TPAPV-NIM-Py-M (2.5-10 μM) under light irradiation). g) Graphical representation of the cell viability of *E. coli* under different treatments. h) Graphical representation of the cell viability of *S. aureus* under different treatments. i) Photographs of crystal violet-stained biofilms treated with TPAPV-NIM-mPy-M and TPAPV-NIM-Py-M under dark or light conditions. j-k) Relative biofilm biomass quantification for TPAPV-NIM-mPy-M (50 μM) and TPAPV-NIM-Py-M (50 μM) under dark or light conditions. Light intensity is 40 mW/cm^2 for panels: a-h, and 85 mW/cm^2 for panels: i-k. (Mean ± SD, $n = 4$), $^*p < 0.05$, $^{**}p < 0.01$, $^{***}p < 0.001$, $^{****}p < 0.0001$, and ns (not significant) as determined by the Student's *t*-test.

components. TPAPV-NIM-mPy-M and TPAPV-NIM-Py-M, with positively charged structures, were expected to exhibit strong binding interactions with the negatively charged surfaces of pathogens, and to substantiate our hypothesis, Gram-positive *S. aureus* and Gram-negative *E. coli* were incubated with the synthesized AIEgens (5 μM) for 30 min at 37 °C under shaking conditions, followed by staining with DNA-staining dye DAPI (20 μM) and observed under a confocal laser scanning microscope. As expected, bright red fluorescence signals were observed from the membranes of both bacterial strains (*S. aureus* and *E. coli*) and blue signals from bacterial DNA (nucleoids), with no overlap with the red signals from the AIEgens, indicating that both AIEgens are bacterial membrane-specific (Fig. 4a-d). To further verify the binding affinity between the synthesized AIEgens and bacteria, zeta potential analysis was performed, which is a sensitive technique for detecting changes in bacterial surface charge upon AIEgen binding. *S. aureus* and *E. coli* were incubated with 5 μM AIEgens for 30 min under shaking conditions at 37 °C, followed by PBS washing, and the changes in the zeta potential were measured using a Zetasizer. The zeta potential of untreated *S. aureus* was −15 mV and shifted toward neutrality after incubation with the AIEgens. Similarly, untreated *E. coli* showed a zeta potential of −25 mV, which shifted to −6 mV and −9 mV after treatment with TPAPV-NIM-mPy-M and TPAPV-NIM-Py-M, respectively (Fig. 4e–f). These changes in surface charge indicate electrostatic interactions between the cationic AIEgens and the negatively charged bacterial envelopes, supporting the strong binding ability of TPAPV-NIM-mPy-M and TPAPV-NIM-Py-M toward both Gram-positive and Gram-negative bacteria.

3.5. In vitro photodynamic therapy

Inspired by the high ROS generation in aqueous solution (Fig. 1) and their strong binding to both Gram-negative and Gram-positive bacteria (Fig. 4), the synthesized PSs were further explored for antibacterial PDT. Intracellular ROS generation is vital for photodynamic inactivation of pathogens, and to evaluate whether the synthesized PSs can generate ROS within bacterial cells, a DCFH-DA staining assay was performed. To detect intracellular ROS, *S. aureus* and *E. coli* were separately incubated with 5 μM of the synthesized AIEgens for 30 min at 37°C with shaking, washed with PBS, and then treated with DCFH-DA (20 μM) for 30 min at 37°C with shaking. Thereafter, the bacterial cells were washed with PBS to remove excess DCFH-DA, irradiated with white light (40 mW/cm^2) for 15 min, and immediately observed under a confocal microscope. Intense green fluorescence signals were observed within the bacterial cells treated with the synthesized PSs, DCFH-DA, and light (Fig. 5a and b), indicating efficient intracellular ROS generation. For comparison, bacterial cells were incubated with DCFH-DA and DAPI, then treated with white light (40 mW/cm^2) for 15 min, and observed under a confocal microscope promptly. No green fluorescence was detected in the control group (Fig. 5a-i and Fig. 5b-i), whereas PS-treated groups showed strong green fluorescence, confirming PS-mediated ROS generation. Membrane-localized ROS generation maximizes oxidative damage to bacterial lipid bilayers while minimizing diffusion into the cytoplasm, thereby enhancing antibacterial efficacy and biosafety.

Given the remarkable intracellular ROS-generating ability of the synthesized PSs, we further evaluated them for *in vitro* PDT using a commonly used plate-counting method. To assess the photodynamic efficacy of TPAPV-NIM-mPy-M and TPAPV-NIM-Py-M against common Gram-negative and Gram-positive pathogenic bacteria (*E. coli* and *S. aureus*), bacterial suspensions with $OD_{600} = 0.1$ were separately incubated with different concentrations (2.5 μM, 5 μM, 7.5 μM, and 10 μM) of TPAPV-NIM-mPy-M and TPAPV-NIM-Py-M to assess dose-dependent phototoxicity of the synthesized PSs toward pathogens, and incubated for 30 min under shaking conditions at 37 °C, followed by PBS washing and white-light irradiation (40 mW/cm^2) for 30 min. To assess the effect of light on bacterial growth, the bacteria-only suspensions ($OD_{600} = 0.1$) were also irradiated with white light (40 mW/cm^2) for 30 min, and to assess the dark toxicity of the synthesized PSs toward bacteria, bacterial suspensions ($OD_{600} = 0.1$) were separately incubated with 10 μM of TPAPV-NIM-mPy-M and TPAPV-NIM-Py-M for 30 min, and used as such without light irradiation. To evaluate the effectiveness of PDT, the light and dark groups were diluted to 1×10^4 CFU/mL, and 70 μL of bacterial suspension was spread onto LB agar plates and incubated for 24 h at 37°C. Bacteria-only suspensions treated with white light were also diluted to 1×10^4 CFU/mL, and a 70 μL suspension was uniformly distributed on the agar plate, followed by incubation at 37 °C for 24 h. Both AIEgens induced dose-dependent phototoxicity in both Gram-negative and Gram-positive bacteria (Fig. 5c-f). TPAPV-NIM-Py-M, with greater ROS generation, effectively eliminated both *E. coli* and *S. aureus* with ~100% killing efficiency; in contrast, TPAPV-NIM-mPy-M, with lower ROS generation, was less effective against *E. coli*, although it also showed ~100% killing efficiency against *S. aureus*. In addition, both AIEgens induced negligible dark toxicity in both *E. coli* and S. aureus. The comparative analysis of cell viability for *E. coli* and *S. aureus* under various treatments is shown in Fig. 5g-h.

3.6. Antibiofilm assay

Bacterial biofilms are surface-associated microbial communities embedded in extracellular polymeric substances (EPSs), consisting of proteins, exopolysaccharides, and extracellular DNA, that shield them from antimicrobial agents and facilitate bacterial survival [3,49,62]. Biofilms, characterized by distinct biochemical conditions, including hypoxia, acidic pH, and elevated levels of hydrolytic enzymes, are responsible for chronic, persistent infections because they exhibit significantly greater resistance to antibiotics, phagocytosis, and immune responses [63]. Research has shown that EPSs not only prevent the effective penetration of antimicrobial agents but also interact with them, reducing their potency and fostering increased resistance [64,65]. Therefore, the ability of antibacterial agents to penetrate and disrupt biofilms is crucial for effectively halting and reversing infection-related damage. To further verify the antibacterial photodynamic activity of the synthesized PSs, we evaluated their antibiofilm activity under light irradiation using a crystal violet staining assay. Preformed *E. coli* and

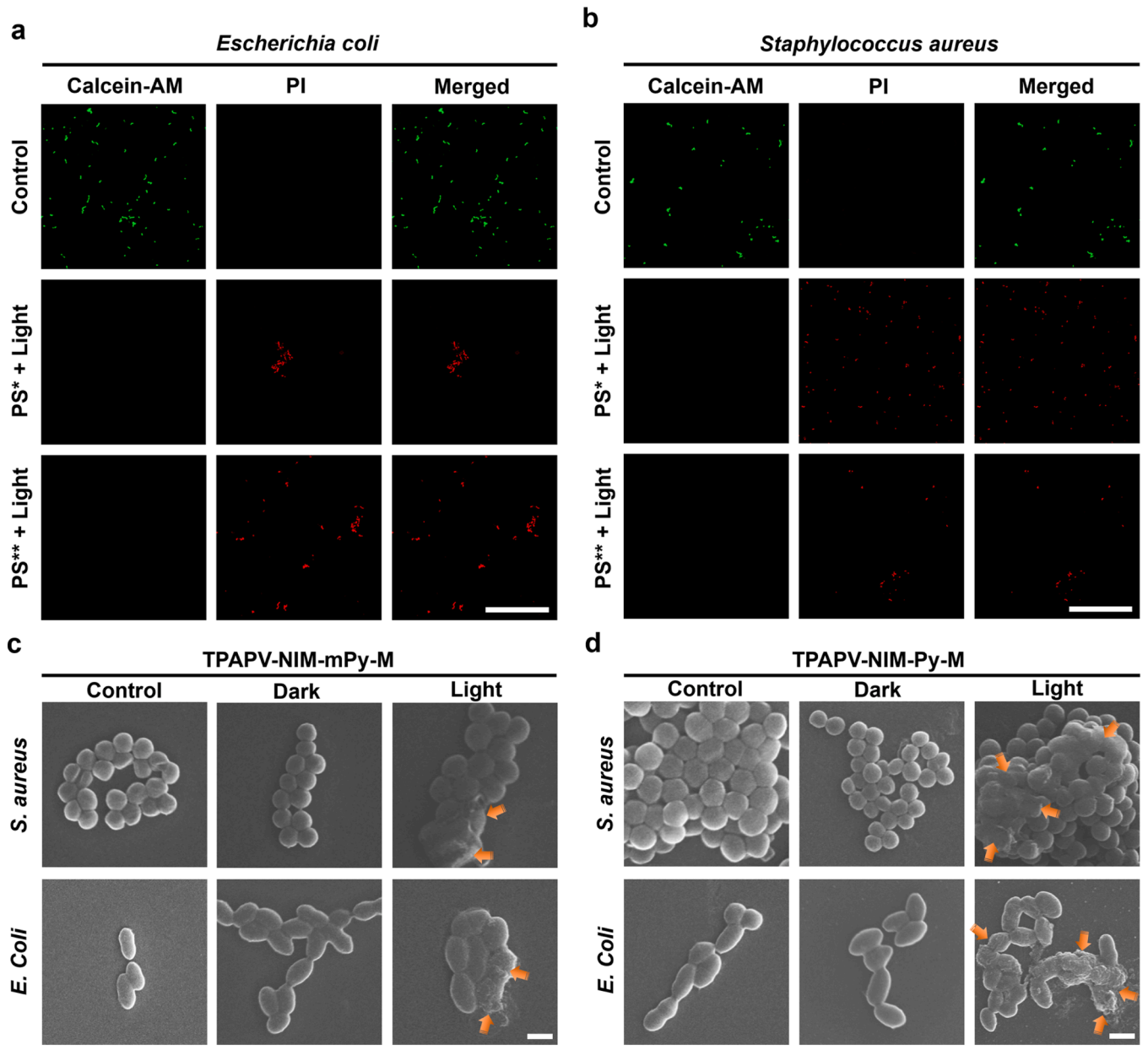

Fig. 6. a) Live/dead cell staining assay in *E. coli* treated with TPAPV-NIM-mPy-M and TPAPV-NIM-Py-M (10 μM) in the absence or presence of white-light irradiation. b) Live/dead cell staining assay in *S. aureus* treated with TPAPV-NIM-mPy-M and TPAPV-NIM-Py-M (10 μM) in the absence or presence of white-light irradiation: Live cells are labeled with calcein-AM (5 μM) with green fluorescence, and dead cells are labeled by PI (15 μM) with red fluorescence. Calcein-AM was excited at 488 nm, and emission was collected between 450 and 700 nm. PI was excited at 561 nm, and the emission was collected between 570 and 700 nm. Light intensity: 40 mW/cm^2. Note: PS* and PS** in Fig. 6a and b denote TPAPV-NIM-mPy-M and TPAPV-NIM-Py-M, respectively. Scale bar: 10 μm. c) SEM images of *E. coli* and *S. aureus* after different treatments: control (*E. coli* or *S. aureus* only + light), dark (*E. coli* and *S. aureus* treated with TPAPV-NIM-mPy-M in the dark), and light (*E. coli* and *S. aureus* treated with TPAPV-NIM-mPy-M and irradiated with white light). d) SEM images of *E. coli* and *S. aureus* after different treatments: control (*E. coli* or *S. aureus* only + light), dark (*E. coli* and *S. aureus* treated with TPAPV-NIM-Py-M in the dark), and light (*E. coli* and *S. aureus* treated with TPAPV-NIM-Py-M and irradiated with white light). Scale bar: 2 μm. Light intensity was 40 mW/cm^2.

S. aureus biofilms were separately incubated with the synthesized PSs (50 μM) for 4 h, then washed with PBS, and the light groups were treated with white light (85 mW/cm^2) for 40 min. After methanol fixation, the biofilms were stained with crystal violet. Both PSs effectively reduced bacterial biofilms under light irradiation (Fig. 5i-k), further supporting their strong photodynamic antibacterial activity.

3.7. Live/dead cell staining assay

To further evaluate the effectiveness of the synthesized PSs in antibacterial PDT, a live/dead cell staining assay was performed using calcein-AM and propidium iodide (PI). PI stains membrane-compromised or dead cells, whereas calcein-AM stains viable cells. To perform the live/dead cell staining assay, bacterial suspensions (*E. coli* and *S. aureus*) with an $OD_{600} = 0.1$ were incubated with 10 μM TPAPV-NIM-mPy-M and TPAPV-NIM-Py-M at 37 °C under shaking conditions (200 rpm) for 30 min, washed twice with PBS, and irradiated with white-light (40 mW/cm^2) for 30 min. Afterward, the bacterial suspensions were stained with PI (15 μM) and calcein-AM (5 μM), and the samples were observed under a confocal microscope immediately. Similarly, for the control group, the bacterial suspensions (*E. coli* and *S. aureus*) with an $OD_{600} = 0.1$ were irradiated with white light (40 mW/

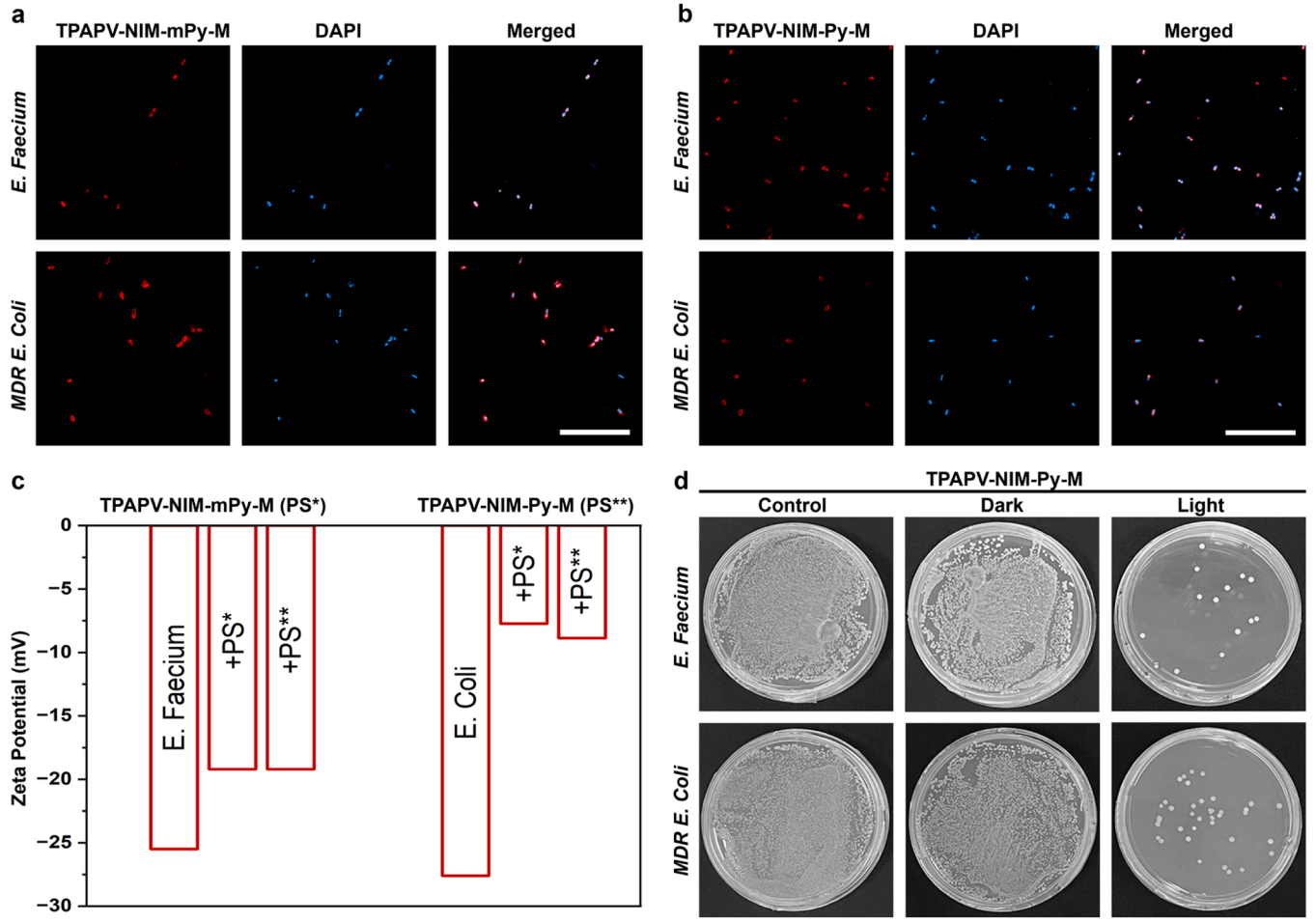

Fig. 7. a) Confocal fluorescence images of VR *E. faecium* and MDR *E. coli* treated with TPAPV-NIM-mPy-M (red fluorescence signals), DAPI (blue fluorescence signals), and merged images. b) Confocal fluorescence images of VR *E. faecium* and MDR *E. coli* treated with TPAPV-NIM-Py-M (red fluorescence signals), DAPI (blue fluorescence signals), and merged images. Scale bar: 10 μm. c) Zeta-potential values of untreated VR *E. faecium* and MDR E. *coli* and those after treatment with TPAPV-NIM-mPy-M or TPAPV-NIM-Py-M. PS* denotes TPAPV-NIM-mPy-M, and PS** denotes TPAPV-NIM-Py-M. d) Survival rates of VR *E. faecium* and MDR *E. coli* under different TPAPV-NIM-Py-M treatments: control (VR *E. faecium* or MDR *E. coli* + light), dark (VR *E. faecium* or MDR *E. coli* treated with TPAPV-NIM-Py-M (10 μM) under dark conditions), and light (VR *E. faecium* or MDR *E. coli* treated with TPAPV-NIM-Py-M (10 μM) under light irradiation).

cm^2), followed by treatment with PI and calcein-AM. No red fluorescence was observed in the control groups, indicating that the bacteria were healthy and that white light had no cytotoxic effect. In contrast, upon white-light irradiation in the presence of the synthesized PSs, bright red fluorescence signals were observed within bacterial cells, indicating efficient photodynamic elimination of bacteria (Fig. 6a-b). Moreover, to visually assess the effectiveness of the synthesized PSs in antibacterial PDT, scanning electron microscopy (SEM) was used. To observe the morphological changes in the bacterial surfaces after PDT, the bacterial suspensions (*E. coli* and *S. aureus*) with an OD_{600} of 0.2 were incubated with 10 μM TPAPV-NIM-mPy-M and TPAPV-NIM-Py-M at 37 °C under shaking conditions, followed by light irradiation (40 mW/cm^2) for 30 min and observation under a scanning electron microscope. Bacterial cell walls were severely damaged in light-treated samples compared with the control groups (dark and bacteria alone) (Fig. 6c-d), further supporting the effectiveness of TPAPV-NIM-mPy-M and TPAPV-NIM-Py-M in photodynamic elimination of pathogens.

3.8. Fluorescence labeling of multidrug-resistant bacteria

We further explored the efficacy of TPAPV-NIM-mPy-M and TPAPV-NIM-Py-M against the clinically isolated VR *E. faecium* (a Gram-positive strain) and standard MDR *E. coli* (a Gram-negative strain). We first evaluated the synthesized PSs for fluorescence labeling of VR *E. faecium* and MDR *E. coli via* confocal laser scanning microscopy. Owing to the positively charged structures of TPAPV-NIM-mPy-M and TPAPV-NIM-Py-M and their strong interactions with common *S. aureus* and *E. coli*, strong binding interactions with drug-resistant bacterial strains were expected, and to substantiate the hypothesis, VR *E. faecium* and standard MDR *E. coli* were separately incubated with the synthesized AIEgens (5 μM) for 30 min at 37 °C under shaking conditions, followed by staining with DAPI (20 μM) and then observed under a confocal laser scanning microscope. As expected, bright red fluorescence signals were observed from the membrane of both bacteria (VR *E. faecium* and MDR *E. coli*) and blue signals from bacterial DNA (nucleoids), with no overlap with the red signals from the AIEgens, indicating that both AIEgens are bacterial membrane-specific (Fig. 7a-b). To further verify the binding affinity between the synthesized AIEgens and drug-resistant bacterial strains, a zeta potential analysis, a sensitive technique for detecting changes in bacterial surface charge upon AIEgen binding, was performed. To perform zeta potential analysis, VR *E. faecium* and MDR *E. coli* were separately incubated with 5 μM of the synthesized AIEgens for 30 min under shaking conditions at 37 °C, followed by PBS washing, and the changes in zeta potential were measured using a Zetasizer.

The zeta potential of untreated VR *E. faecium* was −25.5 mV and shifted to −19.2 mV after treatment with either TPAPV-NIM-mPy-M or TPAPV-NIM-Py-M. Similarly, untreated MDR *E. coli* showed a zeta potential of −27.6 mV, which shifted markedly to −7.74 mV and −8.87

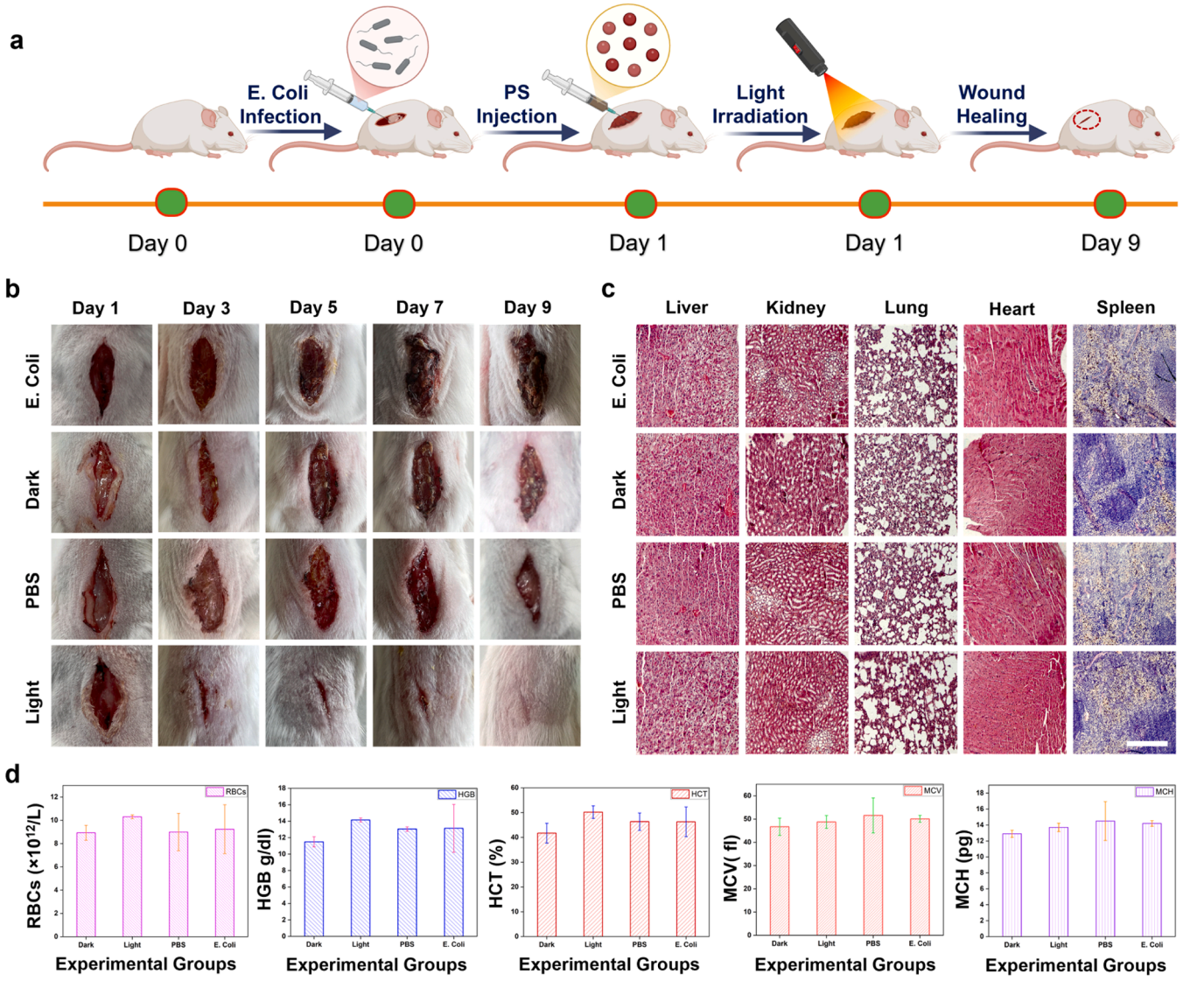

Fig. 8. a) Experimental design and schedule: Day 0 (*E. coli* inoculation), Day 1 (injection of TPAPV-NIM-Py-M and light irradiation), Day 9 (wound-healing experiment completion). b) Photographs of BALB/c mice with *E. coli*-infected wounds under different treatments: *E. coli* (*E. coli* only), dark (*E. coli* treated with TPAPV-NIM-Py-M of 20 μM in the dark), PBS (*E. coli* treated with PBS and white-light irradiation), and light (*E. coli* treated with 20 μM TPAPV-NIM-Py-M under white-light irradiation). c) H&E staining images of vital tissues (liver, kidney, lungs, heart, and spleen) after nine days of treatment in BALB/c mice with *E. coli*-infected wounds. Scale bar: 50 μm. d) Hematological parameters of the blood samples collected from mice of the different treatment groups after nine days of treatment.

mV after incubation with TPAPV-NIM-mPy-M and TPAPV-NIM-Py-M, respectively (Fig. 7c). These changes in surface charge, together with the fluorescence imaging results, support the binding affinity of TPAPV-NIM-mPy-M and TPAPV-NIM-Py-M toward drug-resistant bacterial strains.

3.9. *In vitro photodynamic therapy of multidrug-resistant bacteria*

Owing to its high ROS-generating ability and pronounced *in vitro* photodynamic elimination of common bacterial strains (Fig. 5c-f), we further explored TPAPV-NIM-Py-M against multidrug-resistant bacterial strains (VR *E. faecium* and MDR *E. coli*) using a plate-counting method. To assess the photodynamic efficacy of TPAPV-NIM-Py-M against VR *E. faecium* and MDR *E. coli*, bacterial suspensions with $OD_{600} = 0.1$ were separately incubated with 10 μM of TPAPV-NIM-Py-M, and incubated for 30 min under shaking conditions at 37 °C, followed by PBS washing and white-light irradiation (40 mW/cm^2) for 30 min. To assess the effect of light on bacterial growth, the bacteria-only suspensions ($OD_{600} = 0.1$) were also irradiated with white light (40 mW/cm^2) for 30 min, and to assess the dark toxicity of the synthesized TPAPV-NIM-Py-M against bacteria, bacterial suspensions ($OD_{600} = 0.1$) were separately incubated with 10 μM of TPAPV-NIM-Py-M for 30 min, and used as such without light irradiation. To evaluate the effectiveness of PDT, the light and dark groups were diluted to 1×10^4 CFU/mL, and 70 μL of bacterial suspension was spread onto LB agar plates and incubated for 24 h at 37°C. Bacteria-only suspensions treated with white light were also diluted to 1×10^4 CFU/mL, and a 70 μL suspension was uniformly spread onto an LB agar plate, followed by incubation at 37 °C for 24 h. TPAPV-NIM-Py-M effectively eliminated both VR *E. faecium* and MDR *E. coli* without detectable dark toxicity (Fig. 7d). Based on these results, we conclude that TPAPV-NIM-Py-M exhibits strong phototoxicity against both common and drug-resistant bacterial strains and was further evaluated for *in vivo* antibacterial PDT.

3.10. In vivo photodynamic therapy

Encouraged by the high ROS generation and the remarkable *in vitro* antibacterial efficacy, TPAPV-NIM-Py-M was further evaluated for *in vivo* photodynamic ablation of bacteria *via* a wound-healing experiment in BALB/c mice with *E. coli*-infected wounds. To assess the wound-healing efficacy of TPAPV-NIM-Py-M, a deep incision (~20 mm in length) was performed on the dorsal region of each mouse. The mice were then divided into four groups (n = 3): (1) dark group (*E. coli* + TPAPV-NIM-Py-M), (2) PBS group (*E. coli* + PBS + light), (3) *E. coli* group (*E. coli only*), and (4) light group (*E. coli* + TPAPV-NIM-Py-M + light). At 24 h post-infection with *E. coli*, groups (1) and (4) were administered 20 μM TPAPV-NIM-Py-M by injection into the wounds and kept at room temperature for 3 h, whereas group (2) received only PBS treatment. After 3 h, the PBS and light groups were exposed to white light (~85 mW/cm^2) for 30 min, and the wound-healing process was tracked photographically throughout the PDT experiment. Scars developed on the wounds of the control groups (PBS, *E. coli*, and dark groups) by day 3, while the wounds in the light groups began healing on day 3. The progress of wound healing was monitored until day 9, by which time the wounds in the control groups exhibited minimal closure; in contrast, the light-treated wounds completely healed by day 9, demonstrating the superior photodynamic wound-healing efficacy of TPAPV-NIM-Py-M (Fig. 8b). In addition, the body weights of mice were monitored throughout the PDT experiment, revealing no aberrant changes (Fig. S18), indicating the biosafety of TPAPV-NIM-Py-M for *in vivo* applications.

Next, the biosafety of TPAPV-NIM-Py-M was assessed using hematological analysis and histology of vital tissues collected from mice in the control and light groups. On day 9 of the experiment, blood was collected from all mice; thereafter, they were euthanized, and the vital organs (liver, kidney, lung, heart, spleen) were collected for hematoxylin and eosin (H&E) analysis. According to H&E staining, no pathological abnormalities were observed in tissues collected from mice in either the control or light groups (Fig. 8c), indicating the biosafety of TPAPV-NIM-Py-M. Similarly, the basic hematological parameters, including RBCs, MCV, HGB, MCH, and HCT, in mice treated with TPAPV-NIM-Py-M were within the reference ranges (Fig. 8d), further supporting the biocompatibility of TPAPV-NIM-Py-M for potential translational applications. Taken together, these biosafety results indicate that TPAPV-NIM-Py-M exhibits a favorable biosafety profile and can effectively treat bacterial infections under white-light irradiation.

4. Conclusion

In conclusion, two AIE photosensitizers, TPAPV-NIM-mPy-M and TPAPV-NIM-Py-M, featuring a naphthalimide core and a donor–acceptor architecture, were synthesized via Heck cross-coupling and structurally confirmed by NMR spectroscopy and high-resolution mass spectrometry. Both PSs showed broad visible absorption, NIR fluorescence, AIE characteristics in DMSO/toluene mixtures, and ROS generation through both type I and type II pathways under low-intensity white-light irradiation (27 mW/cm^2). The cationic pyridinium groups promoted strong bacterial binding and membrane localization across Gram-positive and Gram-negative bacteria, enabling effective photodynamic inactivation of *S. aureus* and *E. coli*. Compared with TPAPV-NIM-mPy-M, TPAPV-NIM-Py-M exhibited higher ROS output, likely due to extended π-conjugation, and achieved efficient in vitro antibacterial PDT against vancomycin-resistant *E. faecium* and multidrug-resistant *E. coli*. TPAPV-NIM-Py-M also reduced *E. coli* and *S. aureus* biofilm biomass under light irradiation. TPAPV-NIM-Py-M was further evaluated in an *E. coli*–infected wound model in BALB/c mice, where photodynamic treatment accelerated wound closure and supported tissue regeneration without observable systemic toxicity. Overall, this work highlights membrane anchoring as an effective molecular engineering strategy to improve ROS localization and antibacterial PDT performance, and positions TPAPV-NIM-Py-M as a promising platform for image-guided treatment of common and drug-resistant bacterial infections and infected wounds.

Conflict of interest

The authors declare no competing financial interests.

Supporting Information: The Supporting Information is available free of charge and includes materials and instrumentation, cell culture conditions, drug-resistance profiles of VR *E. faecium* and MDR *E. coli*, synthetic procedures, NMR and HRMS spectra, additional ROS-generation data, theoretical excited-state calculations, and body-weight changes of mice during the wound-healing experiment.

CRediT authorship contribution statement

Sayed Mir Sayed: Writing – original draft, Validation, Investigation, Funding acquisition, Formal analysis, Data curation, Conceptualization. **Zeeshan Tahir:** Writing – original draft, Formal analysis, Data curation. **Yavuz Nuri Ertas:** Writing – review & editing, Writing – original draft, Visualization, Validation, Supervision, Resources, Project administration, Funding acquisition, Conceptualization.

Acknowledgements

This work was supported by the 2232 International Fellowship for the Outstanding Researchers Program of TÜBİTAK (Project No: 121C157). Y.N.E. acknowledges support from the Health Institutes of Türkiye (TÜSEB) Incentive Award, the Turkish Academy of Sciences Distinguished Young Scientist Award (TÜBA-GEBİP), and Scientific and Technological Research Council of Türkiye (TÜBİTAK) Incentive Award.

Supplementary materials

Supplementary material associated with this article can be found, in the online version, at doi:10.1016/j.actbio.2026.06.014.

References

[1] B. Wu, F.Hu Kenry, Targeted antibacterial photodynamic therapy with aggregation-induced emission photosensitizers, Interdiscip. Med. 2 (1) (2024) e20230038.
[2] M.R. Charbonneau, V.M. Isabella, N. Li, C.B. Kurtz, Developing a new class of engineered live bacterial therapeutics to treat human diseases, Nat. Commun. 11 (1) (2020) 1738.
[3] S.M. Sayed, K.-F. Xu, H.-R. Jia, F.-F. Yin, L. Ma, X. Zhang, A. Khan, Q. Ma, F.-G. Wu, X. Lu, Naphthalimide-based multifunctional AIEgens: Selective, fast, and wash-free fluorescence tracking and identification of Gram-positive bacteria, Anal. Chim. Acta 1146 (2021) 41–52.
[4] M.A. Kohanski, D.J. Dwyer, J.J. Collins, How antibiotics kill bacteria: from targets to networks, Nat. Rev. Microbiol. 8 (6) (2010) 423–435.
[5] X.Z. Wu, Z.Y. Xing, H.J. Huang, Z.Y. Ding, Y. Gao, M. Adeli, L. Ma, T. Ma, C. Cheng, C.S. Zhao, Bacteriophage-like nanobiocatalysts with spiky topography and dual-atom sites for treating drug-resistant bacteria, ACS Nano 18 (38) (2024) 26168–26183.
[6] Z.S. Huang, Z. Zhang, Y. Qiu, X. Fang, J. Zhang, H. Gong, S. Wang, L. Yu, X. Ye, Y. Jiang, Elaborately engineered aggregation-induced emission antibacterial agents: negligible living cell invasiveness, efficient bacterial biofilm inhibition and promoting infected wound healing, Small 21 (2025) 2502762.
[7] YY.P. Sun, M.M. Qiu, J.W. Yang, S.T. Wang, T.L. Zhao, D.Y. Lu, B.F. Yan, Z.T. Shao, Y.T. Jiang, Y. Zhang, T.M. Fu, Chlorella pyrenoidosa-based antibiotic liposomal gel promotes wound healing by scavenging biofilm and accelerating regeneration, ACS Appl. Mater. Interfaces 17 (20) (2025) 29132–29145.
[8] YY.P. Wang, X. Zheng, S.Y. Liang, D.Y. Wang, X.J. He, L.X. Pang, Defect-engineered PdOv-TiOX nanozymes with NIR-II responsiveness for synergistic photothermal-chemodynamic therapy of drug-resistant bacterial infections, Chem. Eng. J. 521 (2025) 166943.
[9] D. Yan, Z. Li, M.M. Lee, B.Zhong Tang, D. Wang, NIR-II AIEgens for infectious diseases phototheranostics, Angew. Chem., Int. Ed. 136 (51) (2024) e202414259.
[10] Z.Y. Yue, S. Hussain, Y.N. Feng, C.H. Zhu, C.B. Zhao, C.Q. Liu, X.Y. Liu, Y. Hao, P. C. Ma, R.X. Gao, Aggregation-induced emission-active toroidal micelles from a conjugated polymer: a selective phototheranostic nanoplatform for targeting gram-positive bacteria, ACS Appl. Mater. Interfaces 17 (22) (2025) 32099–32110.

[11] Y.C. Chen, D. Li, X.H. Chen, D.L. Wang, Y. Huang, Y.F. Gao, F. Liu, X.T. Lin, D. G. Zhao, J. Ji, D. Wang, Q. Jin, Side-chain engineering of NIR-II-emissive aggregation-induced emission luminogens to boost photodynamic and photothermal antimicrobial therapy, ACS Nano 19 (16) (2025) 16147–16162.
[12] H.J. Chen, L. Wang, H. Zhu, Z.G. Wang, S.L. Liu, NIR-II fluorescence imaging for quantitative analysis, ACS Appl. Mater. Interfaces 16 (22) (2024) 28011–28028.
[13] T.F. Li, M. Ashrafizadeh, Y.R. Shang, Y.N. Ertas, G. Orive, Chitosan-functionalized bioplatforms and hydrogels in breast cancer: immunotherapy, phototherapy and clinical perspectives, Drug Discov. Today 29 (1) (2024) 103851.
[14] B. Colak, M.C. Cihan, Y.N. Ertas, 3D-printed, implantable alginate/CuS nanoparticle scaffolds for local tumor treatment via synergistic photothermal, photodynamic, and chemodynamic Therapy, ACS Appl. Nano Mater. 6 (17) (2023) 16076–16085.
[15] Z. Wang, H. Liang, A. Liu, X. Li, L. Guan, L. Li, L. He, A.K. Whittaker, B. Yang, Q. Lin, Strength through unity: Alkaline phosphatase-responsive AIEgen nanoprobe for aggregation-enhanced multi-mode imaging and photothermal therapy of metastatic prostate cancer, Chin. Chem. Lett. 36 (2) (2025) 109765.
[16] K.-H. Li, H.-Y. Zhao, D.-D. Wang, M.-H. Qi, Z.-J. Xu, J.-M. Li, Z.-L. Zhang, S.-W. Huang, Mitochondria-targeted nano-AIEgens as a powerful inducer for evoking immunogenic cell death, Chin. Chem. Lett. 35 (5) (2024) 108882.
[17] R. Chen, Y. Liu, Y. Jiang, M. Sun, Z. Fan, J. Du, Recent advances and future prospects in biological-membrane-targeted polymers, Polym. Sci. Technol. 1 (7) (2025) 584–606.
[18] Z. Tahir, S.M. Sayed, E. Lulek, Z.B. Azizoglu, G. Yildiz, E. Balcioglu, A. Cetin, Y. N. Ertas, A near-infrared emitting aggregation-induced emission photosensitizer with endoplasmic reticulum targeting ability for breast cancer photodynamic therapy, ACS Appl. Mater. Interfaces 18 (9) (2026) 13516–13528.
[19] W. Zhou, X. Jiang, X. Zhen, Development of organic photosensitizers for antimicrobial photodynamic therapy, Biomater. Sci. 11 (15) (2023) 5108–5128.
[20] X.M. Hao, J.M. Wu, M. Luo, X.X. Zhai, Y. Liu, Z.X. Gao, Y.R. Liu, Z.Y. Song, S. L. Zhao, J.G. Guan, Mild photothermal-driven nanorobots for infected wound healing through effective photodynamic therapy and wound microenvironment remodeling, Chem. Eng. J. 512 (2025) 162255.
[21] Z.K. Wang, S. Zeng, Y.F. Hao, W.L. Cai, W. Sun, J.J. Du, S.R. Long, J.L. Fan, J. Y. Wang, X.Q. Chen, X.J. Peng, Gram-negative bacteria recognition and photodynamic elimination by Zn-DPA based sensitizers, Biomaterials 308 (2024) 122571.
[22] J.J. Lin, M.Y. Cao, S.Y. Wang, X.Y. Wu, Y.H. Pan, Z.Y. Dai, N.G. Xu, L.M. Zuo, J. Liu, Y.X. Wang, Q.F. Zhong, Y. Xu, J.B. Wu, L.J. Gui, X.Y. Ji, H. Liu, Z.W. Yuan, Deep red-light-mediated nitric oxide and photodynamic synergistic antibacterial therapy for the treatment of drug-resistant bacterial infections, Small 21 (6) (2025) 2408759.
[23] Z. Geng, Z. Cao, J. Liu, Recent advances in targeted antibacterial therapy basing on nanomaterials, Exploration 3 (1) (2023) 20210117.
[24] J. Xie, Y. Wang, W. Choi, P. Jangili, Y. Ge, Y. Xu, J. Kang, L. Liu, B. Zhang, Z. Xie, J. He, N. Xie, G. Nie, H. Zhang, J.S. Kim, Overcoming barriers in photodynamic therapy harnessing nano-formulation strategies, Chem. Soc. Rev. 50 (16) (2021) 9152–9201.
[25] Y.Q. Yang, S.H. Jiang, S.G. Stanciu, H. Peng, A.G. Wu, F. Yang, Photodynamic therapy with NIR-II probes: review on state-of-the-art tools and strategies, Mater. Horiz. 11 (23) (2024) 5815–5842.
[26] W.C. Zhao, L.Q. Wang, M.H. Zhang, Z.Q. Liu, C.B. Wu, X. Pan, Z.W. Huang, C. Lu, G.L. Quan, Photodynamic therapy for cancer: mechanisms, photosensitizers, nanocarriers, and clinical studies, Medcomm 5 (7) (2024) e603.
[27] M. Dirak, C.M. Yenici, S. Kolemen, Recent advances in organelle-targeted organic photosensitizers for efficient photodynamic therapy, Coord. Chem. Rev. 506 (2024) 215710.
[28] S.W. Chen, B.X. Huang, J. Tian, W.A. Zhang, Advancements of porphyrin-derived nanomaterials for antibacterial photodynamic therapy and biofilm eradication, Adv. Healthcare Mater. 13 (27) (2024) 2401211.
[29] J. Yu, W.C. Xu, H. Chen, H.T. Yuan, Y. Wang, X.D. Qian, J. Zhang, Y. Ji, Q. Zhao, S. L. Li, Charge engineering of star-shaped organic photosensitizers enables efficient type-I radicals for photodynamic therapy of multidrug-resistant bacterial infection, Adv. Healthcare Mater. 14 (3) (2025) 2402615.
[30] FF.Y. Xu, T. Cui, J. Wang, W.Z. Li, Y. Gao, X. Li, K. Yang, W.W. Zhang, F. Ge, Y. G. Tao, Quaternized silk fibroin nanocarriers loaded with chlorin e6 for photodynamic elimination of drug-resistant bacteria and biofilms, ACS Appl. Nano Mater. 7 (10) (2024) 12072–12082.
[31] W.J. Wang, Z.Y. Xin, X.X. Su, L. Hao, Z.J. Qiu, K. Li, Y.M. Luo, X.M. Cai, J. Q. Zhang, P. Alam, J. Feng, S.J. Wang, Z. Zhao, B.Z. Tang, Aggregation-induced emission luminogens realizing high-contrast bioimaging, ACS Nano 19 (1) (2025) 281–306.
[32] D.Y. Wei, W.W. Shi, Y.D. Zhao, J.H. Zhang, H.H. Li, X.H. Liu, K. Zhang, J.L. Liu, Spatial distortion-engineered cationic Ru-covalent organic framework overcoming aggregation-caused quenching for synergistic photodynamic/photothermal anti-infective therapy, ACS Appl. Mater. Interfaces 17 (41) (2025) 56786–56801.
[33] H.Y. Wang, X.H. Pan, W.Z. Liu, Y.M. Huang, X.D. Yi, Z. Chen, Bacterial-mediated FRET between AIE and ACQ photosensitizers for enhanced antimicrobial photodynamic therapy, Chem. Eng. J. 486 (2024) 150432.
[34] Z.Q. Huang, J.F. Yang, J.S. Cheng, L.L. Zhou, C.R. Zhao, S. Shen, G. Baryshnikov, H. Ågren, Q. Zou, L.L. Zhu, Molecular engineering of red aggregation-induced emission luminogens with small conjugated structures, Chem. Mater. 36 (17) (2024) 8546–8554.
[35] S.M. Sayed, H.-R. Jia, Y.-W. Jiang, Y.-X. Zhu, L. Ma, F. Yin, I. Hussain, A. Khan, Q. Ma, F.-G. Wu, X. Lu, Photostable AIE probes for wash-free, ultrafast, and high-quality plasma membrane staining, J. Mater. Chem. B 9 (21) (2021) 4303–4308.
[36] S.M. Sayed, X.-F. Li, H.-R. Jia, S. Durrani, F.-G. Wu, X. Lu, A dibenzothiophene core-based small-molecule AIE probe for wash-free and selective staining of lipid droplets in live mammalian and fungal cells, Sens. Actuators B Chem. 343 (2021) 130128.
[37] ZZ.M. Yang, C. Zhang, W.L. Zhang, J.C. Zhong, H.E. Wu, K. Wang, J. Cao, Molecularly engineered high-performance AIE luminogen for NIR-III excitable deep-brain three-photon fluorescence imaging, Chem. Eng. J. 496 (2024) 153741.
[38] X.K. Xue, J. Li, T.J. Chen, M.H. Cui, H.Y. Liang, Y.X. Zhang, M.Q. Xue, H.H. Xiao, J. C. Ge, P.F. Wang, Molecularly engineered NIR-II emitting carbon dots assemblies for unprecedented high-resolution angiography and synergistic photodynamic/photothermal tumor therapy, Chem. Eng. J. 505 (2025) 159356.
[39] D.Y. Yan, D. Wang, B.Z. Tang, In vivo, clinical and translational aspects of aggregation-induced emission, Nat. Rev. Bioeng. 3 (11) (2025) 976–991.
[40] X.R. Chen, Q. Liu, J.J. Zhang, L.J. Tan, J.A. Li, M.L. Ke, B.Z. Tang, Y. Li, Fully inter-restricted assembly of aggregation-induced emission luminogens and polymers enables ultra-bright nanoparticles for sensitive point-of-care diagnosis, ACS Nano 19 (6) (2025) 6221–6235.
[41] S. Xiang, J.X. Li, F.T. Wang, Y. Yang, H.F. Yang, R. Cai, W.H. Tan, Ultrasensitive electrochemiluminescence biosensing platform based on polymer dots with aggregation-induced emission for dual-biotoxin assay, ACS Appl. Mater. Interfaces 16 (29) (2024) 37748–37756.
[42] L. Wang, Y.P. Wei, X.P. Liu, J.S. Chen, C.J. Mao, B.K. Jin, Aggregation-induced enhanced electrochemiluminescence resonance energy transfer biosensor for ultrasensitive detection of carcinoembryonic antigen based on donor-acceptor organic nanoparticles, Langmuir 40 (38) (2024) 20016–20024.
[43] Z. Fang, S. Zhang, W. Wang, Y. Xu, M. Lu, Y. Qian, X. Xiao, Y. Li, B.Z. Tang, M. Zhang, Aggregation-induced emission-based phototheranostics to combat bacterial infection at wound sites: A review, Biomaterials 315 (2025) 122950.
[44] D. Yan, Z. Li, M.M.S. Lee, B.Zhong Tang, D. Wang, NIR-II AIEgens for infectious diseases phototheranostics, Angew. Chem. Int. Ed. 63 (51) (2024) e202414259.
[45] Q. Ding, Y. Xie, K. Xiong, H. Jia, L. Chen, C. Li, Q. Yi, P. Zhang, L. Mei, B.Z. Tang, From light to cure: precision phototherapies for antibiotic-refractory biofilm infections, Angew. Chem. Int. Ed. 64 (43) (2025) e202510900.
[46] J.H. Huang, J. Zhu, S. Xiang, L. Wang, D. Wang, B.Z. Tang, Molecular engineering of AIE-active ionic photosensitizer for dual-organelle targeted NIR-II phototheranostics, Adv. Funct. Mater. 36 (3) (2026) e14187.
[47] T. Yuan, J. Cui, J. Zhu, J. Mei, D. Wang, J.L. Hua, Multi-dimensional donor engineering of NIR-II AIEgens for multimodal phototheranostics of orthotopic breast cancer, Biomaterials 319 (2025) 123193.
[48] M.M.S. Lee, E.Y. Yu, J.H.C. Chau, J.W.Y. Lam, R.T.K. Kwok, B.Z. Tang, Expanding our horizons: AIE materials in bacterial research, Adv. Mate 37 (23) (2025) 2407707.
[49] S.Y. Lv, C. Wang, H. Fu, M.H. Xiao, Z.C. Sun, L. Tian, L.Q. Shi, C.L. Zhu, Synergistic eradication of bacterial biofilms via phage-driven EPS disruption and click-activated AIE photosensitization, Adv. Healthcare Mater. 14 (32) (2025) e02295.
[50] G. Zhong, S. Deng, Y. Hong, F. Zhou, D. Liang, Y. Lin, L. Yang, Y. Guan, C. Pan, L. Yan, L. Zheng, J. Zhang, AIE-active antibacterial photosensitizer disrupting bacterial structure: multicenter validation against drug-resistant pathogens, Small Methods 9 (5) (2025) 2401663.
[51] H. Chen, S. Li, M. Wu, Z.Huang Kenry, C.-S. Lee, B. Liu, Membrane-anchoring photosensitizer with aggregation-induced emission characteristics for combating multidrug-resistant bacteria, Angew. Chem. Int. Ed. 59 (2) (2020) 632–636.
[52] R.N. Jiang, Z.Z. Cai, H.Z.N.W. Bai, Y.L. Liu, B.Y. Zu, X.C. Dou, Precise modulation of the π-conjugated bridge of naphthalimide-based probes for high-performance fluorescent sensing of H_2O_2, Anal. Chem. 97 (22) (2025) 11669–11677.
[53] H. Zhou, Z. Zhu, H.Y. Guo, L.B. Lin, X.T. Fang, F.F. Yang, Naphthalimide-tetraaryl imidazopyridinium: an effective fluorescent probe for detecting lambda-cyhalothrin, Microchem. J. 218 (2025) 115418.
[54] C. Geraghty, C. Wynne, R.B.P. Elmes, 1,8-Naphthalimide-based fluorescent sensors for enzymes, Coord. Chem. Rev. 437 (2021) 213713.
[55] H. Zhu, C. Liu, M. Su, X. Rong, Y. Zhang, X. Wang, K. Wang, X. Li, Y. Yu, X. Zhang, B. Zhu, Recent advances in 4-hydroxy-1,8-naphthalimide-based small-molecule fluorescent probes, Coord. Chem. Rev. 448 (2021) 214153.
[56] A.S. Oshchepkov, M.S. Oshchepkov, M.V. Oshchepkova, A. Al-Hamry, O. Kanoun, E.A. Kataev, Naphthalimide-based fluorescent polymers for molecular detection, Adv. Opt. Mater. 9 (6) (2021) 2001913.
[57] J. Feng, X. Jian, G. Jiang, J. Wang, Charged aggregation-induced emission luminogens for bioimaging and phototherapy, Luminescence 39 (1) (2024) e4669.
[58] T. Xiong, Y. Chen, M. Li, X. Chen, X. Peng, Recent progress of molecular design in organic type I photosensitizers, Small 21 (22) (2025) 2501911.
[59] G. Song, T. He, R. Wang, Y. Ouyang, N. Jain, S. Liu, B. Kan, Y. Shang, J. Li, X. Wang, Z. Yao, X. Wan, C. Li, W. Ma, Y. Zhao, G. Long, C. Zhang, F. Gao, Y. Chen, Regulate the singlet–triplet energy gap by spatially separating HOMO and LUMO for high performance organic photovoltaic acceptors, Angew. Chem. Int. Ed. 64 (35) (2025) e202506357.
[60] Y. Yin, X. Cheng, D. Fan, Y. Fang, H. Li, X. Zhou, H. Guo, W. Zeng, F. Chen, Harnessing membrane-targeting photosensitizers to evoke ferroptosis and pyroptosis dual-modal cell death for antitumor therapy, Mol. Pharmaceutics 22 (10) (2025) 6302–6316.
[61] X. Yang, X. Wang, X. Zhang, J. Zhang, J.W.Y. Lam, H. Sun, J. Yang, Y. Liang, B. Z. Tang, Donor–acceptor modulating of ionic AIE photosensitizers for enhanced ROS generation and NIR-II emission, Adv. Mater. 36 (28) (2024) 2402182.
[62] Y.-Y. Xie, Y.-W. Zhang, X.-Z. Liu, X.-F. Ma, X.-T. Qin, S.-R. Jia, C. Zhong, Aggregation-induced emission-active amino acid/berberine hydrogels with enhanced photodynamic antibacterial and anti-biofilm activity, Chem. Eng. J. 413 (2021) 127542.

[63] P. Liu, D. Li, M. Kang, Y. Pan, Z. Wen, Z. Zhang, D. Wang, B.Z. Tang, Emerging applications of aggregation-induced emission luminogens in bacterial biofilm imaging and antibiofilm theranostics, Small Struct 4 (5) (2023) 2200329.
[64] M. Xiao, K. Xue, H. Fu, J. Wang, S. Lv, Z. Sun, C. Wang, L. Shi, C. Zhu, Photodynamic patterning of living bacterial biofilms with high resolutions for information encryption and antibiotic screening, Aggregate 5 (4) (2024) e532.
[65] SS. Wu, C. Xu, Y. Zhu, L. Zheng, L. Zhang, Y. Hu, B. Yu, Y. Wang, F.-J. Xu, Biofilm-sensitive photodynamic nanoparticles for enhanced penetration and antibacterial efficiency, Adv. Funct. Mater. 31 (33) (2021) 2103591.